Bioactive Materials 37 (2024) 459–476

Contents lists available at ScienceDirect

Bioactive Materials

journal homepage: www.keaipublishing.com/en/journals/bioactive-materials

Nanofiber-induced hierarchically-porous magnesium phosphate bone cements accelerate bone regeneration by inhibiting Notch signaling

Jingteng Chen [a,1], Ling Yu [a,1], Tian Gao [b,1], Xiangyang Dong [c], Shiyu Li [a], Yinchu Liu [a], Jian Yang [a], Kezhou Xia [a], Yaru Yu [a], Yingshuo Li [a], Sen Wang [a], ZhengFu Fan [b,*], Hongbing Deng [c,**], Weichun Guo [a,***]

[a] Department of Spine Surgery, Renmin Hospital of Wuhan University, Wuhan, 430060, China
[b] Key Laboratory of Carcinogenesis and Translational Research (Ministry of Education/Beijing), Department of Bone and Soft Tissue Tumor, Peking University Cancer Hospital and Institute, Beijing, 100142, China
[c] Hubei Key Laboratory of Biomass Resource Chemistry and Environmental Biotechnology, Hubei International Scientific and Technological Cooperation Base of Sustainable Resource and Energy, School of Resource and Environmental Science, Wuhan University, Wuhan, 430079, China

ARTICLE INFO

Keywords:
Critical-sized bone defects
Magnesium phosphate bone cement
Silk fibroin nanofibers
Bone regeneration
Notch signaling pathway

ABSTRACT

Magnesium phosphate bone cements (MPC) have been recognized as a viable alternative for bone defect repair due to their high mechanical strength and biodegradability. However, their poor porosity and permeability limit osteogenic cell ingrowth and vascularization, which is critical for bone regeneration. In the current study, we constructed a novel hierarchically-porous magnesium phosphate bone cement by incorporating extracellular matrix (ECM)-mimicking electrospun silk fibroin (SF) nanofibers. The SF-embedded MPC (SM) exhibited a heterogeneous and hierarchical structure, which effectively facilitated the rapid infiltration of oxygen and nutrients as well as cell ingrowth. Besides, the SF fibers improved the mechanical properties of MPC and neutralized the highly alkaline environment caused by excess magnesium oxide. Bone marrow stem cells (BMSCs) adhered excellently on SM, as illustrated by formation of more pseudopodia. CCK8 assay showed that SM promoted early proliferation of BMSCs. Our study also verified that SM increased the expression of OPN, RUNX2 and BMP2, suggesting enhanced osteogenic differentiation of BMSCs. We screened for osteogenesis-related pathways, including FAK signaing, Wnt signaling and Notch signaling, and found that SM aided in the process of bone regeneration by suppressing the Notch signaling pathway, proved by the downregulation of NICD1, Hes1 and Hey2. In addition, using a bone defect model of rat calvaria, the study revealed that SM exhibited enhanced osteogenesis, bone ingrowth and vascularization compared with MPC alone. No adverse effect was found after implantation of SM *in vivo*. Overall, our novel SM exhibited promising prospects for the treatment of critical-sized bone defects.

1. Introduction

Critical-sized bone defects, most frequently caused by high-energy trauma, bone tumor resection, or osteomyelitis, pose substantial challenges to orthopedic surgeons in terms of disease management [1]. Although autologous bone and allograft bone are essential in treating critical-sized bone defects, they have inherent drawbacks including limited availability of donor bone sources, immunological rejection, and

Peer review under responsibility of KeAi Communications Co., Ltd.
* Corresponding author.
** Corresponding author.
*** Corresponding author.
E-mail addresses: jtchen@whu.edu.cn (J. Chen), scaling@126.com (L. Yu), gaotianauagcu@163.com (T. Gao), xiangyangdong@whu.edu.cn (X. Dong), 2314304604@qq.com (S. Li), 786890328@qq.com (Y. Liu), yangjian1986@whu.edu.cn (J. Yang), xiakz0617@163.com (K. Xia), yaruyu@whu.edu.cn (Y. Yu), liyingsrhuo@whu.edu.cn (Y. Li), senwang2003@whu.edu.cn (S. Wang), zff_bjcancer@126.com (Z. Fan), hbdeng@whu.edu.cn (H. Deng), guoweichun@aliyun.com (W. Guo).
[1] These authors contributed equally to this work.

https://doi.org/10.1016/j.bioactmat.2024.03.021
Received 24 December 2023; Received in revised form 11 March 2024; Accepted 15 March 2024

potential transfer of infectious diseases [2,3]. Polymethyl methacrylate (PMMA) bone cement is a commonly employed bone filler that possesses exceptional mechanical characteristics. Nevertheless, its clinical application is restricted because to its elevated elastic modulus, intense heat generation during polymerization, and non-biodegradability. In addition, PMMA is biologically inert and exhibits unsatisfactory osseointegration characteristics [4,5]. Calcium phosphate bone cements (CPC) have attracted significant interest as synthetic substitutes for bone repair due to their chemical and structural resemblance to real bone, lack of toxicity, and good biocompatibility [6,7]. However, the limited mechanical strength, slow biodegradation, and low osteoinductivity of CPC hinder its widespread use in orthopedics [8]. Therefore, it is extremely important and of great interest to create advanced bone substitutes for the purpose of repairing bone defects [9,10].

Recent studies indicate that bioceramics emit magnesium ions (Mg) that have the ability to induce the differentiation of osteoblast precursor cells through signaling pathways involving growth factors [11]. Among the Mg-based bioactive scaffolds, magnesium phosphate bone cements (MPCs) are the most commonly researched in the field of bone healing and reconstruction [12]. It is reported that MPCs function well in bone defect repair owing to their superior properties including fast solidification, high initial strength and suitable biodegradability [13]. Kanter et al. found that MPCs showed potential for stimulating bone repair of significant bone defects in large animals [14]. Our previous studies also indicated that MPCs improved new bone formation by integrating gelling systems *in vitro* and *in vivo* [15–17]. Nevertheless, certain constraints are associated with MPC, such as its small pore structure, low porosity, elevated pH levels and inadequate biocompatibility resulting from the increased presence of magnesium oxide (MgO) residues. To be more explicit, the absence of a hierarchically-porous structure impedes the invasion of osteogenic cells and the formation of blood vessels [18]; additionally, the strongly alkaline environment caused by the magnesium oxide (MgO) residues severely impairs the biocompatibility of MPC [19]; furthermore, MPCs lack organic nanofibrous components similar to those found in the bone extracellular matrix (ECM) which could lead to better outcomes for bone repair [10]. Thereupon, new modification strategies should be explored to get novel satisfied MPC with suitable physiochemical performance, great bioactivity as well as biomimetic properties.

Nanofibers are increasingly being recognized as versatile materials that exhibit exceptional mechanical and chemical characteristics [20]. Additionally, studies have shown that fibers possess the ability to impact the structure within scaffolds. For example, Cai et al. developed a reinforced CPC by adding nanofibers which provided the cement with a microporous structure and rough surface [21]. Fang et al. designed a scaffold that incorporates fibers and has a hierarchical structure, providing optimal porosity for effective cell seeding [22]. Silk fibroin (SF) nanofibers have gained considerable attention in tissue engineering owing to their distinctive mechanical properties, adjustable biodegradation rate, and capacity to facilitate the differentiation of mesenchymal stem cells [23]. Studies have also shown that SF has the ability to generate an acidic environment during decomposition, which can counteract the alkaline nature of MPC [24]. Notably, SF nanofibers possess a hierarchical suprafibrillar structure like that of organic matrix in the ECM of natural tissue [25,26]. Several studies have demonstrated utilization of SF to construct the ECM of tissues such as liver, cartilage and intervertebral discs, confirming its applicability in clinical medicine [27–29]. Consequently, SF nanofibers were chosen as additives to create a hierarchically-porous scaffold by combining them with MPCs. However, a thorough investigation is still needed to determine the precise impacts and possible processes of the materials' biological reaction.

Notch signaling is a key factor in regulating cell fate and in numerous developmental processes through the translation of specific transcriptional programs from cell–cell interactions [30]. The role of Notch signaling in osteogenesis has been examined through numerous *in vitro* and *in vivo* studies. Notch signaling exerts its skeletal function in a temporally- and spatially-dependent manner [31]. Kraus et al. discovered that activation of Notch signaling in the initial stages of bone healing in the zebrafish mandible enhances the transformation of callus into reparative bone [32]. Meanwhile the utilization of γ-secretase inhibitors also accelerated the production of bone callus [33]. These findings indicate that the Notch signaling pathway plays a pivotal and multifaceted role in bone regeneration. It is reported that inhibition of Notch signaling is essential for inducing the expression of osteogenic genes in silk-based scaffolds [34]. However, the mechanism by which SM control osteogenesis through the modulation of Notch signalling is unclear.

In this study, we developed a novel composite by incorporating SF nanofibers into MPC (SF nanofibers–MPC, SM). SF nanofibers endowed MPC with improved physico-chemical properties, especially with hierarchically-porous structure and lower pH. We confirmed that SM could promote BMSCs adhesion, proliferation and osteogenic differentiation *in vitro*. The osteogenic mechanisms of addition of SF nanofibers on Notch signaling was also investigated. As verified by critical-sized defects in rat calvaria, SM enhenced osteogenesis and angiogenesis compared with MPC. Collectively, the current study provided a successful approach for managing critical-sized bone defects (Scheme 1).

2. Results and discussion

2.1. Characterization of SM scaffold

Electrospinning is widely acknowledged as the preferred method of producing nanofibers for tissue engineering applications due to the morphological and structural similarities of the resulting nanofibers to the natural ECM [20]. In the present study, electrospun SF nanofiber mats were embrittled and ground to obtain short nanofibers. They were then evenly blended with MgO and KH_2PO_4 to form the solid phase, and finally mixed with the liquid phase, deionized water, to form the SF nanofiber-magnesium phosphate cement scaffold (SM scaffold) (Fig. 1A). The nanofibers obtained by electrospinning exhibited a normal distribution with a diameter of 619.98 ± 95.40 nm and formed a palisade-like structure by linking to each other, which was reported to be more favorable for the adherence of cells (Fig. 1B–D) [20].

Energy dispersive X-ray spectroscopy (EDS) and the X-ray photoelectron spectra (XPS) tests were performed to determine the primary elements of the material. The EDS spectra revealed the presence of nitrogen (N) peaks in SM scaffolds, in addition to carbon (C), oxygen (O), magnesium (Mg), phosphorus (P), and potassium (K) peaks, compared to those of MPC (Fig. 1E, F and Figs. S1A and B). Consistent with the findings from EDS, XPS examination revealed a significant increase in N content in SMs compared with MPC as the increase of the SF content. Furthermore, the alteration in binding energy was not consistent, and the introduction of SF had minimal impact on the binding energy of the remaining constituents (Fig. S2). The observed increase in N originated from SF, indicating that SF was effectively integrated into MPC, however it had no impact on the reaction of MPC. X-ray diffraction (XRD) and Fourier-transform infrared spectroscopy (FTIR) were further utilized to analyze the prepared SM scaffolds. The diffraction peaks of XRD confirmed that all the specimens contained a mixture of K-struvite ($KMgPO_4{\cdot}6H_2O$) and unreacted MgO (with peaks at 42.98° and 62.36°) (Fig. 1G). All groups displayed identical diffraction peaks, suggesting that the incorporation of SF did not have any significant impact on the crystallization of MPC. According to the FTIR analysis, the characteristic absorption peaks in SF appeared at 1657 cm^{-1} (amide I, C═O stretching), 1535 cm^{-1} (amide II, N–H deformation vibration), and 1241 cm^{-1} (amide III, N–H variable angle and C–H stretching vibration) reflecting α-helix and random coil structures in SF [35]. In the MPC spectrum, we observed the characteristic absorption peaks of Mg–O stretching vibrations (572 cm^{-1}) and PO_4^{3-} stretching (1010 cm^{-1}) [36]. The FTIR spectra of SM-35 scaffold exhibited the absorption peaks of both SF and MPC, demonstrating that SF was successfully incorporated into MPC

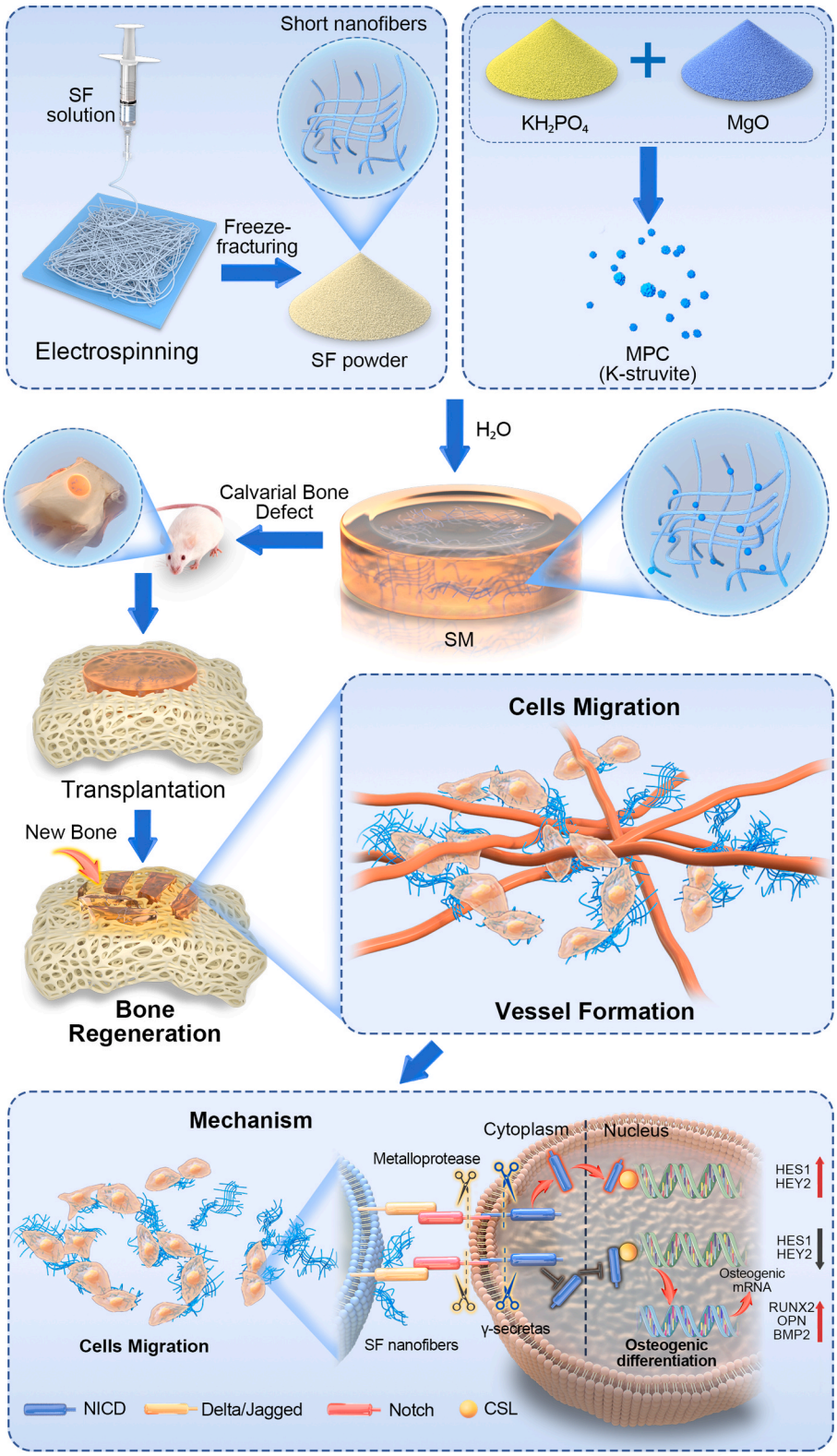

Scheme 1. Schematic representation of SM for repairing bone defects. Firstly, the methodology and procedural steps involved in SF powders and SM fabrication were presented. Additionally, the *in vivo* bone repair capability was estimated using a rat calvaria defect model. Finally, molecular mechanism through which SM faciliateds bone regeneration by suppressing the Notch pathway was elucidated.

(Fig. 1H). The microstructure of these scaffolds was observed using electron microscopic scanning. It can be seen that a multitude of criss-cross nanofibers was found on the surface and inside the SM-35 (Fig. 1I–K), which provided a higher surface-to-volume ratio and thus facilitated better attachment of cells compared to MPC [35].

In our previous study, MPC showed excellent injectability, especially when modified by carboxymethyl chitosan and sodium alginate [15]. However, it was difficult to inject SM paste through a syringe, as the

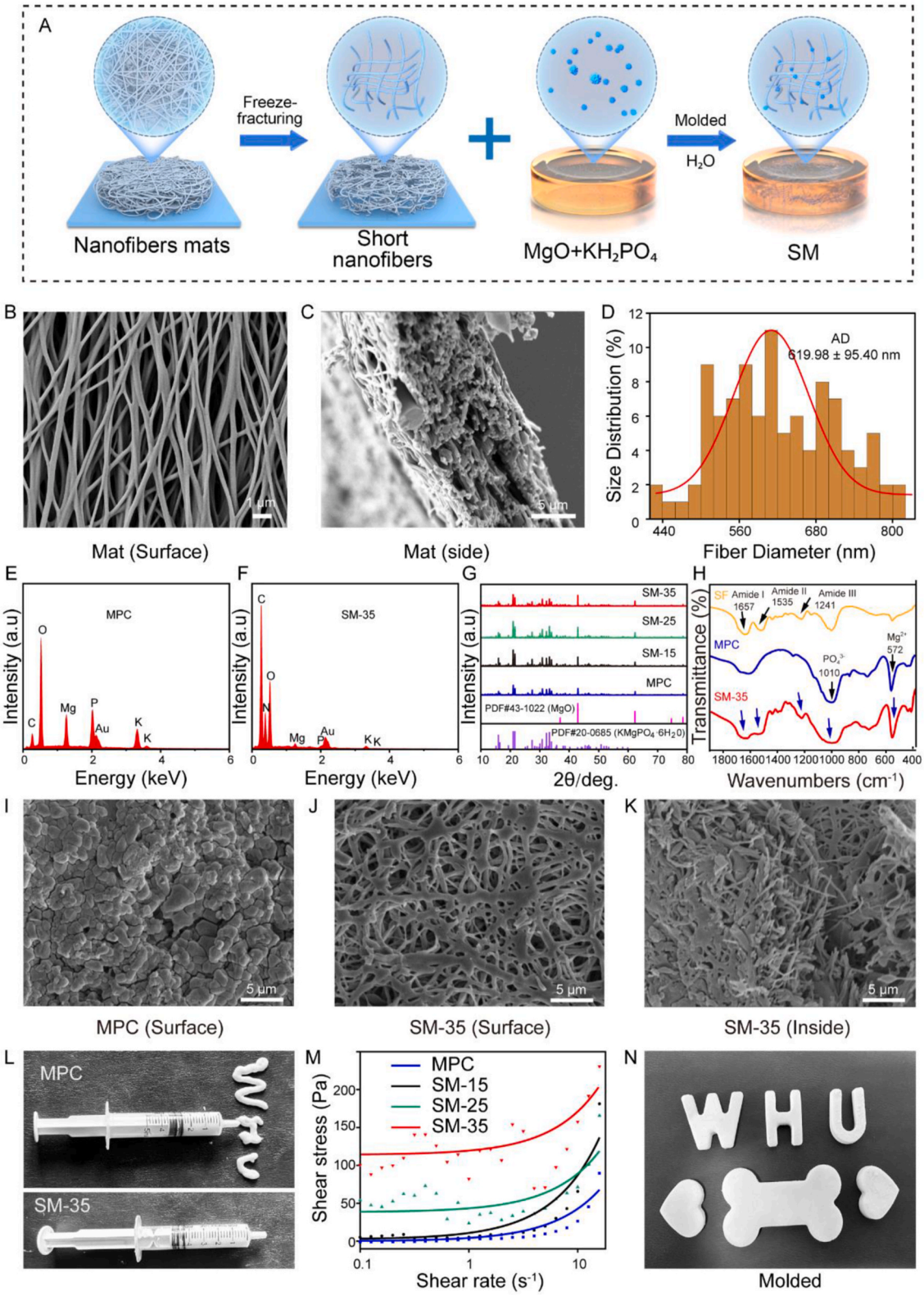

Fig. 1. Characterization of SM scaffold. (A) Schematic illustration of the fabrication procedure of SM. (B) and (C) Surface and side morphology of SF nanofibers. (D) Average diameter (AD) of SF nanofibers. (E) and (F) EDS analysis of the elemental composition of MPC and SM-35. (G) XRD results from cements after 3 days of setting (primary diffraction peaks of $KMgPO_4·6H_2O$ and MgO, denoted by (◆) and (◊), respectively). (H) FTIR spectra of SF, MPC, and SM-35 after 3 days of setting. Blue arrows indicate absorption peaks of SM-35, which appear in either the SF or MPC (Black arrows). (I) Surface morphology of MPC captured by THF-SEM. (J) Surface morphology of SM-35 captured by THF-SEM. (K) Interior structure of SM-35 at high magnification captured by THF-SEM. (L) Injectability of MPC and non-injectable SM-35. (M) Rheological property of MPC, SM-15, SM-25, SM-35. (N) Molded SM.

unresolvable fibers are likely to block the outlet (Figs.1L). The rheological properties of bone cement are crucial for assessing the injectability of a prepared mixture [37]. The rheological properties of the cement slurry were then assessed using a rotational rheometer. It was observed that the inclusion of SF led to an elevation in the shear stress of the cement slurry, with the shear stress increasing proportionally to the SF content. In other words, the addition of SF negatively impacts the injectability of the cement (Fig. 1M). However, SM scaffold can be fabricated into any shape using a mold (Fig.1N), which implies that bone defects with irregular shapes can be completely filled with SM scaffold.

2.2. Physicochemical properties of SM scaffold

Mimicking the natural extracellular matrix (ECM) is an important criterion for selecting the optimal scaffold for bone repair [38]. It is reported that bone ECM consists of ~35% organic components [39]. We previously added carboxymethyl chitosan and chondroitin sulfate into MPC to imitate the bone ECM. These organic polymers functioned as a gel network to enhance the physicochemical characteristics and osteogenic potential of MPC [15,17,36]. However, the maximum amount of these polymers added into MPC could not exceed 10%. In this study, we initially set the groups as SM-15, SM-25, SM-35 and SM-45. It has been reported that the addition of fibers reinforces the composite, increasing its mechanical strength [40]. For example, Zhu et al. fabricated a glass fiber-reinforced polyvinyl alcohol hydrogel composite, which exhibited desirable mechanical performance in cartilage repair [41]. Cai et al. designed a novel calcium phosphate bone cement with enhanced mechanical performance by adding poly(lactide-co-glycolic acid) nanofibers to the solid phase [21]. Therefore, the mechanical strength of these samples were subsequently detected. Consistently, we found that the addition of SF nanofibers increased the compressive strength of MPC, and SM-35 reached the 38.14 ± 5.18 MPa, which was almost double that of MPC alone (22.29 ± 2.63 MPa) (Fig. 2A). The rationale for the improved mechanical performance is as follows. First, the fibers created a consistent structural framework, which effectively restricted the occurrence of further fractures through fiber bridging and crack deflection (Fig. 2C a-b). In addition, it demonstrated resilience against compressive stress by efficiently dispersing energy across the entire matrix , namely frictional sliding (Fig. 2C c) [40,42]. However, the compressive strength decreased as the amount of SF nanofibers continued to increase. In detail, SM-45 shattered at 150 N and it was fragile and can hardly molded. This could be explained by the fact that the excess SF became agglomerated, so that the cement became difficult to mold (Fig. 2C d). In addition, the increase in porosity further decreased the mechanical strength. Thus, it is unnecessary to detect the other properties of SM-45.

The determination of an appropriate setting time is of the utmost importance in clinical application [15]. It is generally accepted that the suitable setting time for handling during operation is about 10–15 min [43]. In the current study, it was found that the initial and final setting time of the SM scaffold decreased significantly as the quantity of SF nanofibers grew. The initial setting time was reduced from 7.82 ± 0.30 min to 6.08 ± 0.23 min, and the final setting time was reduced from 16.30 ± 2.79 min to 12.42 ± 0.65 min (Fig. 2B). This decrease could be due to the penetration of the liquid phase into the interstices of the nanofiber bundles, resulting in a decrease in the liquid-to-solid ratio and hence a faster setting of the MPC [21,44]. In fact, the setting time of MPC can be significantly affected by the composition of the material. In our previous studies, the duration of the setting process for MPC was extended by incorporating a gelling system, including carboxymethyl chitosan and chondroitin sulfate. Carboxymethyl chitosan readily formed membranes to envelop the composite surface, resulting in deceleration of the hydration reaction. In contrast, chondroitin sulfate, characterized by a substantial negative charge density, facilitated the nucleation of Mg^{2+} ions [15,17]. Nevertheless, they were still within the range of clinical requirements [21,45]. The temperature also has a significant impact on the setting time, with higher temperature resulting in shorter setting time [46]. We then utilized a thermal infra imaging apparatus to quantify the exothermic profiles of the cements. Our findings indicated that the maximum temperature rose from 67.5 ± 0.46 °C (MPC) to 68.27 ± 0.29 °C (SM-35) as the SF concentration increased. Additionally, the time needed to attain the maximum peak temperature decreased from 885 s (MPC) to 510 s (SM-35) (Fig. S3). These indicated that SF content had an obvious impact on the hydration speed, which resulted in a shorter setting time and earlier exothermic performance.

The biodegradability of MPC is a significant advantage in comparison to traditional CPC [47,48]. It was noted that the degradation in different SM scaffolds soaking in PBS was generally similar (Fig. 2D). After 28 days, the mean weight loss rate of MPC reached 18.93 ± 1.37%. Meanwhile, MPC containing SF degraded relatively slowly, with the mean weight loss rates of SM-15, SM-25 and SM-35 being 18.42 ± 0.99%, 17.10 ± 2.15% and 18.19 ± 0.35% respectively, after 28 days. No statistically-significant differences were found between these groups. In order to substantiate this finding, we also observed the deterioration characteristics of the cements while immersed in Simulated Body Fluid (SBF) (Fig. S4). The average rate of weight loss for MPC after 28 days was 18.60 ± 0.46%. The average weight loss rates for SM-15, SM-25, and SM-35 were 18.45 ± 0.65%, 18.16 ± 0.39%, and 18.01 ± 0.41% correspondingly, during a period of 28 days. No significant statistical differences were seen between these groups.

In the MPC system, excess unreacted MgO increases the amount of OH^- in the surrounding environment causing it to become inordinately alkaline, which is not suitable for cell growth and may result in inflammatory reactions [18]. In this study, the pH value curves showed that all cement-soaked media were alkaline, and the pH value gradually increased with increased soaking time (Fig. 2E). The pH value of each group increased rapidly in the first seven days, implying the rapid reaction of MgO and water, whereas it increased slowly and gradually stabilized later. Notably, the pH value of MPC decreased after the addition of SF. The effect was most significant in the SM-35 group, which had a pH value of 7.98 ± 0.24 at day 28, approximately 2 units less than that of MPC (Fig. 2E). Furthermore, in order to reflect the influence of the cement on the pH of physical conditions, we measured the pH change using simulated body fluid (SBF). We found that the pH value of each group in SBF had similar trend as to PBS, however, a smaller variation of the pH was observed due to its strong buffer system in SBF (Fig. S5).According to the literature, the lowered pH, at nearly 7.8, may enhance the process of bone regeneration in osteoporotic bone by inhibiting the activity of aberrant osteoclasts [49]. Several methods have been confirmed to decrease the pH of MPC, such as decreasing the Mg/P ratio or mixing acidic substances [17]. Indeed, we utilized a low Mg/P ratio of 1.5:1 rather than the commonly used 2:1 ratio. Additionally, the decreased pH upon mixing with SF nanofibers might be due to their anionic groups, such as carboxyl, which have a similar effect to that of chondroitin sulfate used in our previous study [17,50].

Another advantage of MPC is that it gradually degrades and releases magnesium ions [51]. The polymer matrix is permeable to water, which facilitates the diffusion of Mg^{2+} from the scaffolds. Our investigation revealed that the presence of SF did not have any impact on the release of Mg^{2+} within the concentration range of 15–35%. Furthermore, the release of Mg^{2+} was approximately in direct proportion to the degradation of the cement, and the precipitation of Mg^{2+} exhibited a tendency to remain steady (Fig. S6).

2.3. Hierarchically-porous structure of the SM scaffold

In the present study, we observed that the incorporation of SF nanofibers resulted in a hierarchically-porous structure in the SM scaffold. The porosity increased with the addition of SF nanofibers, and SM-35 displayed a porosity of 45.40 ± 2.83% (Fig. 3A). In accordance with previous publications, porosity affects the mechanical qualities of

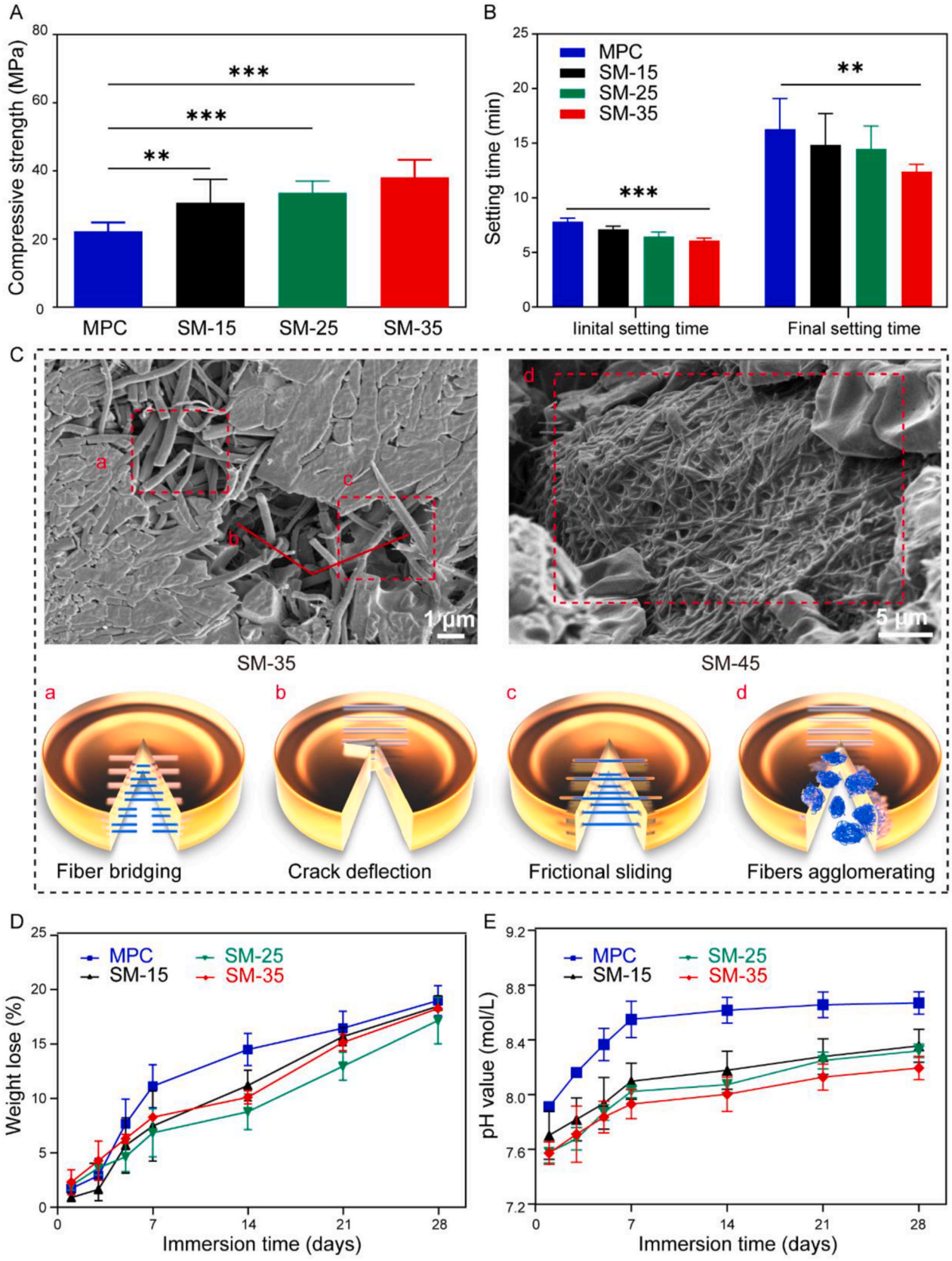

Fig. 2. Effects of SF nanofibers on the physiochemical properties of MPC. (A) Compressive strength of MPC, SM-15, SM-25, and SM-35. (B) The initial and final setting time of MPC, SM-15, SM-25, and SM-35. (C) Schematic illustration of impact factors of SM-35 (fiber bridging (a), crack deflection (b) and frictional sliding (c)) and schematic illustration of fibers agglomerating in SM-45 (e). (D) Evolution of the weight loss of MPC, SM-15, SM-25, and SM-35 after immersion in PBS at different time points. (F) The pH vibration of PBS after cement soaking at different time points. The data are shown as mean ± SD with a specimen number of at least three; statistical significance compared to the MPC group, $*p < 0.05$, $**p < 0.01$ and $***p < 0.001$.

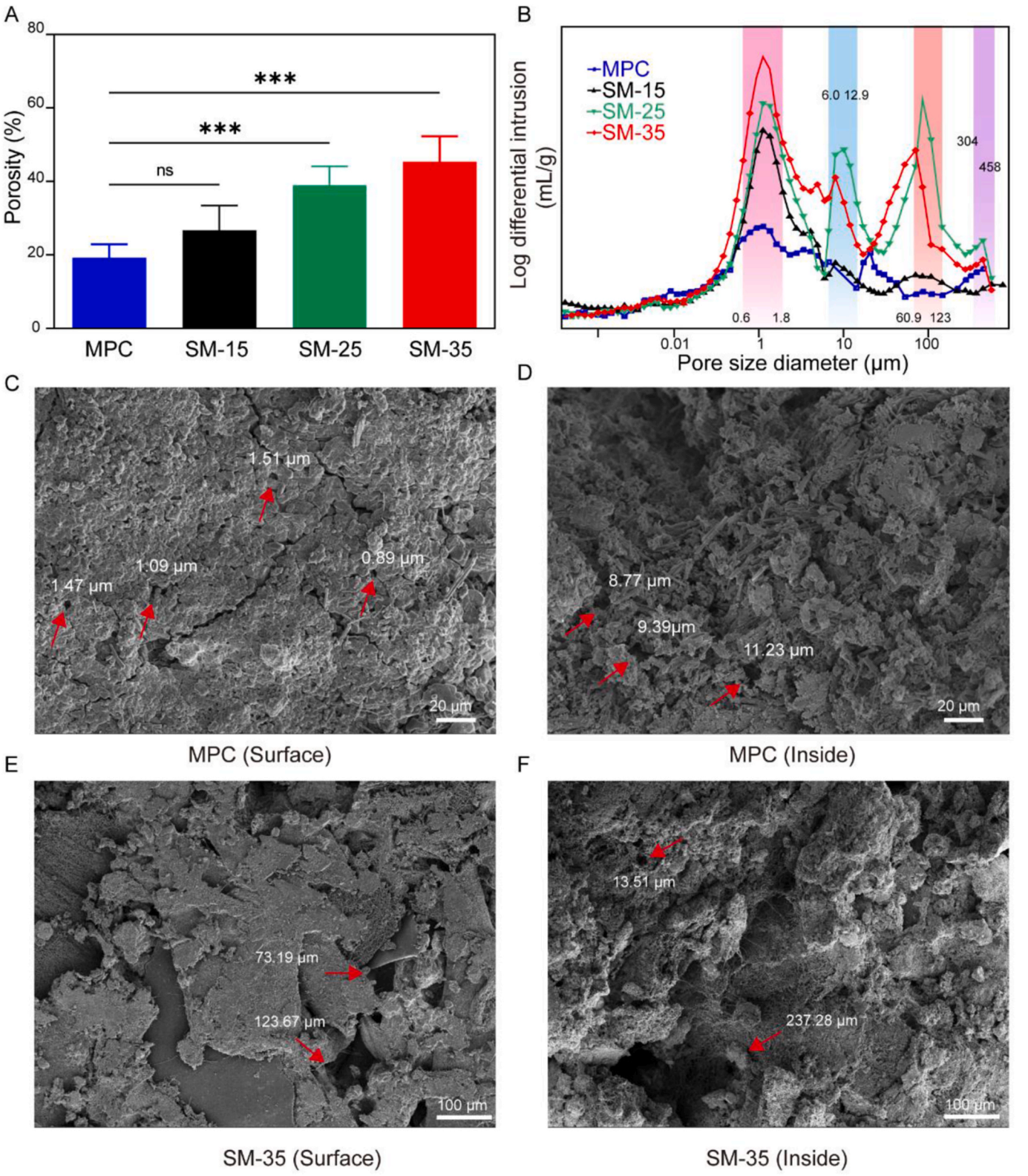

Fig. 3. Effects of SF nanofibers on the hierarchically-porous structure of SM. (A) Porosity of MPC, SM-15, SM-25, and SM-35. (B) Pore size distribution of MPC, SM-15, SM-25, and SM-35. (C) Surface morphology of MPC captured by THF-SEM. (D) Interior structure of MPC captured by THF-SEM. (E) Surface morphology of SM-35 captured by THF-SEM. (F) Interior structure of SM-35 captured by THF-SEM. Red arrows indicate the pore structure of different samples. The data are shown as mean ± SD with a specimen number of at least three; statistical significance compared to the MPC group, $^{*}p < 0.05$, $^{**}p < 0.01$ and $^{***}p < 0.001$.

cement, with a higher porosity corresponding to a lower compressive strength [15]. As mentioned above, our porous SM scaffolds are able to withstand external loading stresses as long as the SF nanofibers constitute less than 45 wt% of the scaffold. Further, we used the mercury intrusion porosimetry (MIP) test to assess the pore size distribution of the SM scaffolds. We found that there was a single peak in the MPC group with pore diameter around 1 μm. When SF nanofibers increased to 15%, the number of pores around 1 μm increased extremely, which contributed to facilitate the attachment of proteins and the communication of ions. Intriguingly, three new peaks (6.0–12.9 μm, 69–123 μm, and 304–458 μm) appeared when SF nanofibers exceeded 25%, which aided to the formation of fibrous tissue without mineralization (pores ≤50 μm), regeneration of mineralized bone (pores ≥50 μm) and vascularization during the formation of new bone tissue (pores ≥400 μm) [52,53]. MIP testing of SM-35 revealed similar pore size distributions to SM-25 (Fig. 3B). We also observed that different size of pores were present in SM scaffolds by tungsten hairpin filament scanning electron microscopy (THF-SEM). We could see that many small pores with consistent size of around 1 μm were distributed over the surface of the MPC. Pores within the MPC were larger but still only had a diameter of around 10 μm (Fig. 3C and D). However, hierarchical sized pores could clearly be detected on the surface and within the interior of SM-35. Typical pores with diameters of 13.51 μm, 73.19 μm, 123.67 μm and 237.28 μm are indicated by the red arrows, and these results are very similar to the results of MIP (Fig. 3E and F).

The pore structure could be affected by adding fibers into the scaffolds [54]. Kim et al. previously produced a concrete with many large pores by incorporating twisted fibers because the fibers interfere with the distribution of aggregates and contribute to enlargement of the pores [55]. Another study introduced a ceramic composite with hierarchical structure reinforced by short SiC fibers [56]. Consistent with these findings, our results confirmed the hierarchically-porous structure

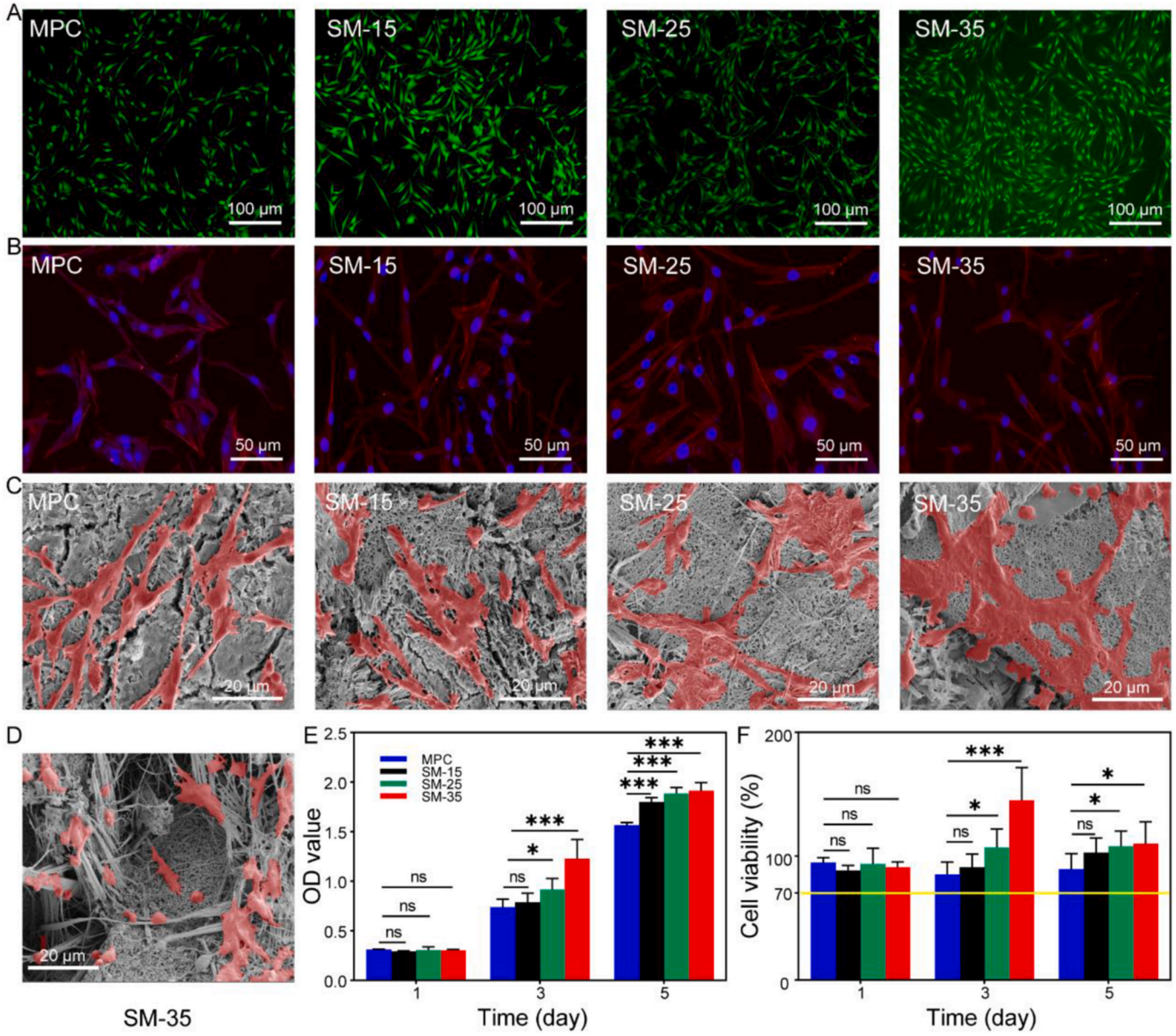

Fig. 4. Biocompatibility of BMSCs co-cultured with bone cements. (A) Live/dead assay of BMSCs. (B) Immunofluorescence staining of the cytoskeleton of BMSCs stained by TRITC-phalloidin. (C) Morphology of BMSCs on the surface of cements visualized by THF-SEM after 24 h incubation. (D) Morphology of BMSCs in the pores of cements visualized by THF-SEM after 24 h incubation. (E) CCK8 analysis of BMSCs at days 1, 3 and 5. (F) Cell viability of BMSCs of MPC, SM-15, SM-25 and SM-35 at days 1, 3 and 5 calculated according to OD value. Line of OD value (cell viability) = 70% was marked in yellow. The data are shown as mean ± SD with a specimen number of at least three; statistical significance compared to the MPC group, $^{*}p < 0.05$, $^{**}p < 0.01$ and $^{***}p < 0.001$.

created by nanofiber incorporation, which makes it suitable for different needs in bone regeneration.

2.4. SM scaffold promotes adhesion and proliferation of BMSCs

The *in vitro* biocompatibility of SM scaffolds was further evaluated. The majority of cells in all specimens exhibited excellent viability, and no obvious dead cells (red color) were recorded under the microscope (Fig. 4A). To investigate the attachment of the BMSCs on the SM scaffolds, TRITC phalloidin staining and THF-SEM were performed. The microfilament skeletons of the BMSCs in all groups were clearly observed (Fig. 4B), and SEM results demonstrated that the cells spread well in all groups and SEM results demonstrated that the cells spread well in all groups (Fig. 4C). Additionally, it was apparent that the cells on the SM scaffolds exhibited more pseudopodia compared to those on MPC, suggesting better adhesion to the scaffold (Fig. 4C). What's more, our study revealed that BMSCs were capable of effectively infiltrating and adhering to the pores of SM-35 (Fig. 4D). The optical density (OD) value obtained from the CCK-8 assay demonstrated that the BMSCs exhibited robust vitality and efficient proliferation across each experimental group (Fig. 4E and F). Significantly, SM-35 consistently shown the highest level of proliferative capacity in comparison to the other groups. By the fifth day, the cell viability of SM-35 had decreased compared to the third day, however the cells were still growing rapidly. This enhanced biocompatibility could be attributed to the nanoscale fibers fabricated by electrospinning, which offered several benefits, such as resemblance to the structure of ECM in native bone, providing a high surface/volume ratio for cell attachment and organization, and a less alkaline environment [20]. For instance, one study created a mimicked SF hydrogel with dispersed electrospun SF nanofibers and silica nanoparticles. This hydrogel served as the foundation for the composite scaffold to imitate the ECM and demonstrated an improved osteoinductive function [28]. Another study used SF scaffolds enhanced with SF-chitin hybrid nanofibers, which mimicked the ECM to boost cartilage

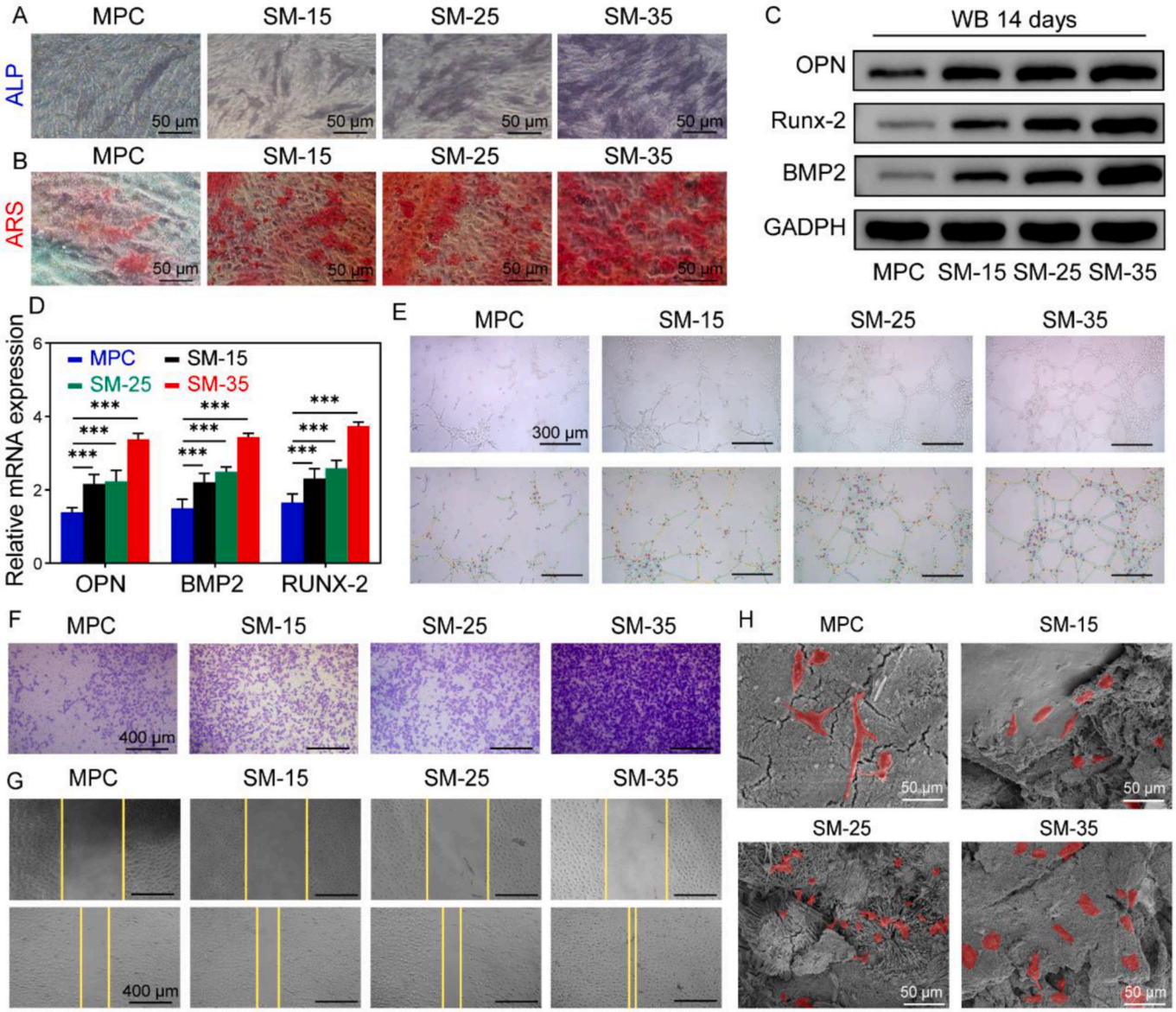

Fig. 5. Osteoinductive effects on BMSCs co-cultured with bone cements. (A) ALP staining of BMSCs after 14 days of culture. (B) ARS staining of BMSCs after 21 days. (C) ALP activity of BMSCs after 14 days. (D) Quantitative analysis of ARS staining. (E) Expression of osteogenesis-related proteins (BMP2, RUNX-2 and OPN) by BMSCs co-cultured with bone cements assessed after 14 days. (F) Quantitative analysis of western blotting. (G) Osteogenesis-related gene expression (BMP2, RUNX-2 and OPN) by BMSCs co-cultured with bone cements for 14 days. The data are shown as mean ± SD with a specimen number of at least three; statistical significance compared to the MPC group, $*p < 0.05$, $**p < 0.01$ and $***p < 0.001$.

regeneration [35]. Overall, these findings indicated that SM scaffold possessed excellent biocompatibility and supported cell adhesion and proliferation.

2.5. SM scaffold mediates osteogenic differentiation of BMSCs

The osteogenic ability of SM was then examined. After 14 days of co-culture with bone cement, BMSCs showed positive results for alkaline phosphatase (ALP) staining in all groups. Additionally, the more SF nanofibers were added, the stronger the ALP expression (Fig. 5A). Accordingly, the ALP activity exhibited a comparable pattern (Fig. S7A). Alizarin red S (ARS) staining was conducted to assess the deposition of calcium phosphate of BMSCs co-cultured with bone cement (Fig. 5B and Fig. S7B). Notably, the SM-35 sample exhibited the greatest deposition of mineral, as demonstrated by both the number and area of calcium nodules. The calcium nodules of SM-25 were similar to those of SM-15. Consistently, SM significantly promoted the expression of these markers compared with MPC, with SM-35 exhibiting a distinct improvement (Fig. 5C–D and Fig. S7C).We therefore confirmed that SM promotes the osteogenic differentiation of BMSCs. However, its detailed effects and the potential mechanism remain to be systematically investigated.

2.6. SM scaffold induces angiogenesis of human umbilical vein endothelial cells (HUVECs)

The material's influence on angiogenesis was assessed using HUVECs. Based on the results of the tube formation evaluation, we observed an improvement in the development of tubular structures following the addition of SF (Fig. 5E). The quantitative data obtained using Image J software indicated that the number of master junctions increased by 59.00 ± 7.00%, 65.67 ± 6.66%, and 86.00 ± 8.54% after 12 h of treatment, respectively, compared to the MPC group (36.67 ± 6.11%) (Fig. S8A). The overall segment length experienced a rise of 8234.00 ± 447.00, 9061 ± 1032.00, and 13674.00 ± 334.70 in the SM-15, SM-25, and SM-35 groups, respectively, compared to the MPC group (6118.00 ± 233.70) after a 12-h treatment (Fig. S8B). The Transwell assay demonstrated an increased number of cells that migrated across the membrane into the bottom chamber, indicating a more robust migratory response of HUVECs to SMs (Fig. 5F and Fig. S8C). In the wound healing model *in vitro*, it was consistently observed that the migratory ability of HUVECs was increased by 46.45 ± 4.30%, 48.75 ± 4.96%, and 85.40 ± 3.78% in the SM-15, SM-25, and SM-35 groups, respectively, compared to the MPC group (20.76 ± 1.73%) (Fig. 5G and Fig. S8D). The THF-SEM images (Fig. 5H) caught the attachment of HUVECs to various cement surfaces. These images demonstrated that the surfaces of SMs offered a superior adhesive surface for HUVECs. All of these findings indicate the beneficial impact of SMs on angiogenesis.

2.7. The Notch pathway plays a key role in SM-mediated osteogenesis

Previously, we demonstrated that the focal adhesion kinase (FAK) –Wnt axis is involved in reinforced osteogenic differentiation of MPC-carboxymethyl chitosan-alginate [36]. To explore whether FAK-Wnt axis functions similarly in SM, we analyzed the protein expression of FAK, phosphorylated-FAK (p-FAK), β-catenin and phosphorylated-β-catenin (p-β-catenin) by western blotting and gene expression by qRT-PCR, and found that there were no significant differences in the expression of these proteins or genes between MPC and SM groups (Fig. 6A–C). Previous study reported that Notch signaling negatively regulated osteogenesis on silk based matrices [34]. Jung et al. confirmed that low molecular weight silk fibroin peptides leaded to enhanced expression of ALP and Runx2 mRNA by significantly suppressing Notch signaling in bone marrow cells [57]. Thus we speculated that SM might promote bone regeneration by modulating Notch signaling. Subsequently, we detected the Notch pathway-related proteins and genes in cells co-cultured with different scaffolds. Consistently, we found that the expression levels of NICD1 and the downstream target genes Hes1 and Hey2 were all down-regulated in the SM groups, especially in SM-35 (Fig. 6D–F).

Notch signaling plays a key role in skeletal homeostasis through the regulation of osteogenesis. However, several *in vitro* and *in vivo* studies yield conflicting results on the Notch pathway regulated osteoblast differentiation. Early in 2008, Hilton et al. found that Notch signaling maintained bone marrow mesenchymal progenitors by suppressing osteoblast differentiation using several mouse strains that Notch were genetically disrupted [58]. At the same time, Engin et al. found that gain of Notch function activated expansion of the immature osteoblastic pool and inhibited differentiation by repressing Runx2 [59]. In 2015, Wang et al. also found that gamma-secretase inhibitor (GSI) significantly enhanced bone callus formation via the promotion of MSC differentiation [33]. The same group also reported that removal of Notch signaling resulted in depletion of the BMSC pool, which implied the requirement for Notch and BMSCs in fracture repair [60]. The above studies suggest that Notch maintains BMSCs population, while inhibition of Notch promotes osteogenic differentiation. On the contrary, Kraus et al. found that Notch signaling enhanced bone regeneration in the zebrafish mandible, while inhibition of Notch signaling reduced the size of the cartilage callus and delayed its conversion into bone [32]. Remark et al. also observed that loss of Notch activity displayed elevated skeletal stem and progenitor cells and enhanced bone repair [61]. These discrepancies could be due to temporal and spatial dependence of Notch pathway in cell fate determination. To further elucidate the role of the Notch signaling pathway in effecting the osteogenic function of SM, BMSCs (SM-35) and BMSCs over-expressing NICD1 (OE-NICD1) were co-cultured with SM-35 (SM-35+OE-NICD1). BMSCs transfected with lentivirus control were set as the negative control (SM-35+sham). The cells in the SM-35+OE-NICD1 group showed lower expression of OPN and RUNX-2 compared with SM-35 alone (Fig. 6G–I). In addition, SM-35+OE-NICD1 exhibited weaker ALP expression, lower ALP activity and a lesser degree of mineralization (Fig. 6J–M). However, there were no significant differences in the expression of OPN, Runx-2, or ALP, ALP activity or ARS staining between SM-35 and SM-35+sham. Therefore, we concluded that SMs enhanced osteogenesis by suppressing the Notch signaling pathway.

2.8. SM scaffold promotes bone defect repair in vivo

SM-35 was selected for *in vivo* research because of its good biocompatibility, greatest ability to induce osteogenic differentiation of BMSCs *in vitro* among the SMs and its superior compressive strength compared to other groups (Fig. S9). Micro-CT was used to determine the new bone formation and scaffold degradation in the defect area. Micro-CT scanning and the 3D reconstructed images of typical samples showed scattered regenerated osseous tissue in both the SM-35 and MPC groups 4 weeks after the operation. However, at 12 weeks after implantation, the SM-35 group exhibited significantly better bone formation and a faster degradation rate than the MPC group (Fig. 7A and B). The degradation rate of SM cements *in vivo* was determined by analyzing the data obtained from reconstructed micro-CT (Fig. S10). After four weeks following the operation, the degradation rate of MPC was measured to be 10.66 ± 3.17%, whereas the degradation rate of SM-35 was found to be 13.84 ± 4.56%. After being implanted for a duration of 12 weeks, the MPC material underwent degradation of 54.36 ± 4.37%, whereas the SM-35 material had degradation of 60.56 ± 4.72%. Specifically, the addition of SF hastened the breakdown of MPC *in vivo*. Additionally, after 4 weeks, the structural parameters showed similarity in both groups. (Fig. 7C–F). Significantly higher BV/TV, Tb.N, and Tb.Th values were observed in the SM-35 group compared to the MPC group 12 weeks after transplantation (51.20 ± 4.24% vs. 42.22 ± 4.00%, and 1.90 ± 0.36 mm vs. 1.29 ± 0.11 mm and 0.44 ± 0.05 mm vs. 0.38 ± 0.03 mm, respectively). Conversely, the Tb.Sp value of the SM-35 group was significantly lower than that of the MPC group (0.32 ± 0.07 mm vs. 0.41

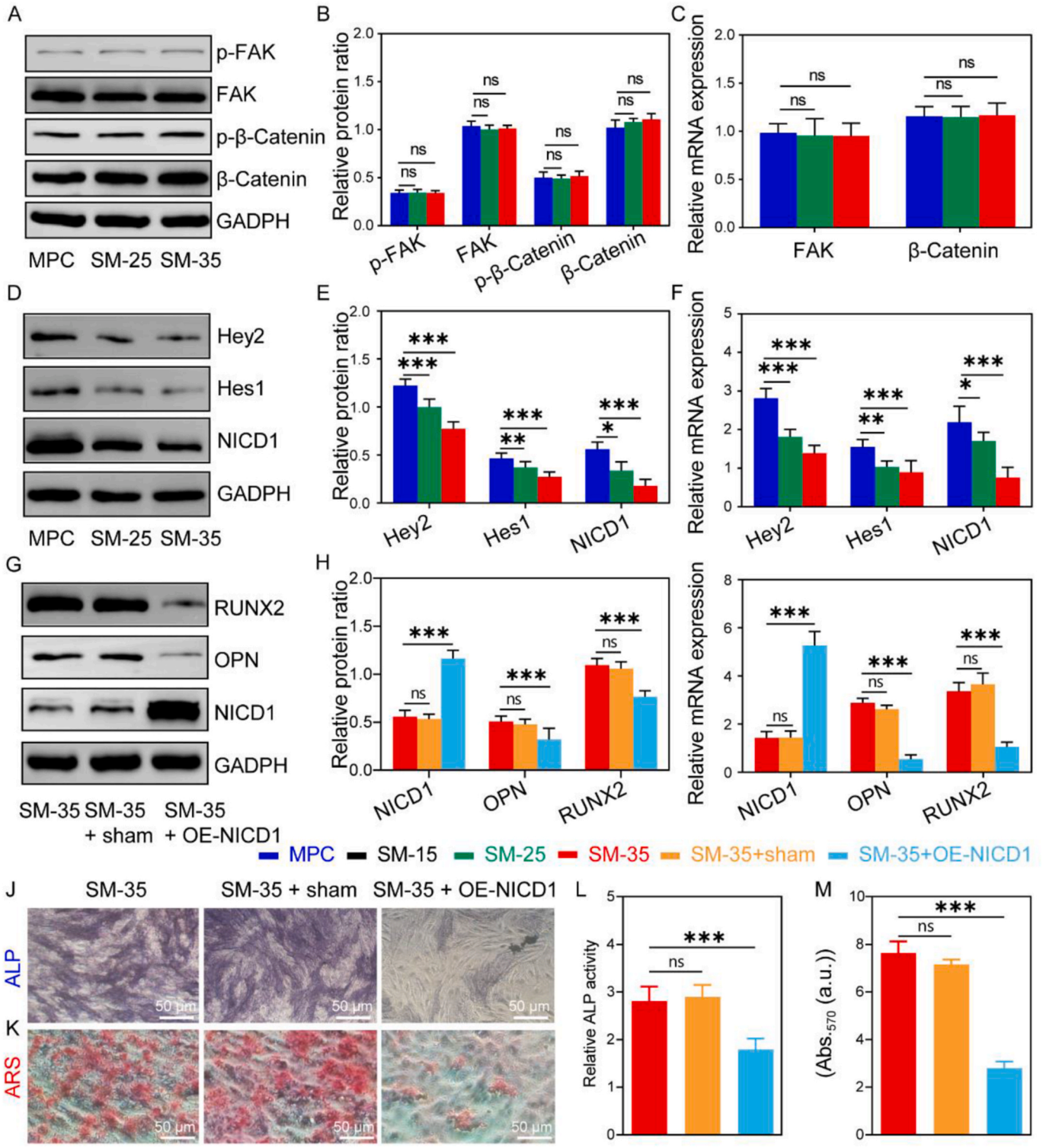

Fig. 6. Mechanism detection of the bone healing effect of SM. (A) Expression of FAK–Wnt axis-related proteins (FAK, p-FAK, β-catenin and p-β-catenin) by BMSCs co-cultured with bone cements over 14 days. (B) Quantitative analysis of western blotting. (C) Expression of FAK-Wnt axis-related genes (FAK, p-FAK, β-catenin and p-β-catenin) by BMSCs co-cultured with bone cements over 14 days. (D) Expression of Notch signaling pathway-related proteins (NICD1, Hes1, and Hey2) by BMSCs co-cultured with bone cements over 14 days. (E) Quantitative analysis of western blotting. (F) Expression of Notch signaling pathway-related genes (NICD1, Hes1, and Hey2) by BMSCs co-cultured with bone cements over 14 days. Western blotting (G) and (H), qRT-PCR (I), ALP staining (J), ALP activity (L), and ARS staining (K) and (M) of BMSCS co-cultured with SM-35 showing the influence of osteogenic differentiation on activated Notch signaling. The data are shown as mean ± SD with a specimen number of at least three; statistical significance compared to the MPC group, $*p < 0.05$, $**p < 0.01$ and $***p < 0.001$.

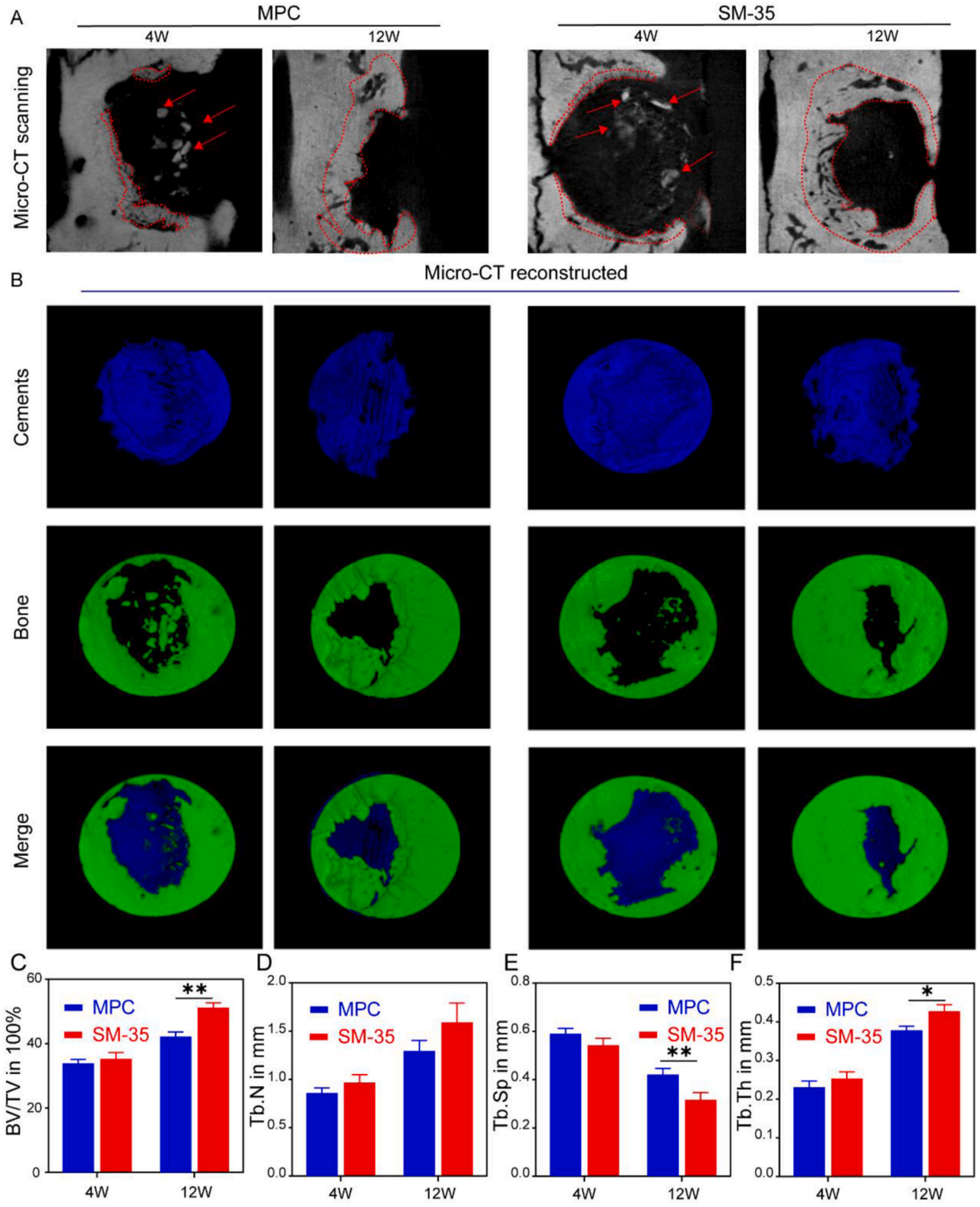

Fig. 7. Abilities of different cements to regenerate bone after being implanted into a rat cranial bone defect. (A) Rat calvarial bone defects imaged by micro-CT scanning after implantation of MPC and SM-35 at 4 and 12 weeks (newly regenerated bone is shown circled by a red dotted line; red arrows indicate the scattered callus). (B) 3D constructed images from micro-CT scans of MPC and SM-35 at 4 and 12 weeks (blue: cements; green: newly-regenerated bone) (C–F) Micro-CT measurements of the quantities of BV/TV, Tb.N, Tb.Sp and Tb.Th in the rat calvaria bone defects. TV: total tissue volume; BV: bone volume; BV/TV: volume ratio; Tb.N: trabecular bone number; Tb.th: trabecular bone thickness; Tb.Sp: trabecular separation. The data are shown as mean ± SD with a specimen number of at least three; statistical significance compared to the MPC group, $*p < 0.05$, $**p < 0.01$ and $***p < 0.001$.

± 0.08 mm). The grater of the value of Tb.Sp, the more osteoporotic it is [62]. Therefore, these results indicate the strong promotion of bone healing by SM-35.

The bone–implant interfaces were evaluated using hematoxylin and eosin (H&E) and Masson's trichrome staining at 4 and 12 weeks post-implantation. H&E staining revealed the absence of inflammation, necrosis, or infection at the graft sites, further indicating a high level of biocompatibility of the bone cement (Fig. 8A–D). Both MPC and SM-35 demonstrated the capacity for bone regeneration after 4 weeks, as evidenced by the initiation of callus formation. However, some of the connective tissue was still present at the defect site (Fig. 8A and B). At the 12 weeks following implantation, SM-35 exhibited a significant greater degree of dense calcification in the newly-regenerated bone. Additionally, the cement used in SM-35 exhibited a more rapid deterioration rate than that used in MPC (Fig. 8C and D). However, no signs of defect healing were observed in the control group (Fig. S11).

To provide more proof of the osteogenic effects of the SM scaffold, immunofluorescence analysis was conducted to identify the presence of OPN expression. At 4 weeks after implantation, only a few newly formed OPN-positive cells were observed in both SM-35 and MPC. However, SM-35 exhibited a higher quantity of OPN-positive cells compared to MPC after 12 weeks. (Fig. 8E and H).

To evaluate the speed at which bone mineralization occurs, a series of intraperitoneal injections of ARS were given after the surgery. The decision was based on the capacity of fluorochromes to attach to calcium ions in newly formed bone, thus becoming part of the particular area that is undergoing mineralization [63]. The findings from the fluorescent labeling of mineralization demonstrated that the SM-35 and MPC groups had similar intervals between the fluorescent signals after 4 weeks. However, the SM-35 group exhibited a wider interval between the fluorescent signals at 12 weeks, suggesting a more rapid progression of new bone formation (Fig. 8F). Quantitative analysis was conducted to evaluate the mineral apposition rate (MAR) (Fig. 8I). At 4 weeks and 12 weeks after implantation, the MAR of the MPC group was 0.12 ± 0.06 μm/day and 0.28 ± 0.08 μm/day, respectively. For the SM-35 group, the MAR values were 0.17 ± 0.05 μm/day and 0.36 ± 0.14 μm/day at the corresponding time points. Notably, at 4 weeks and 12 weeks following implantation, the MAR of the SM-35 group was considerably greater than that of the MPC group. All these indicated that SM-35 facilitated bone repair more quickly than the conventional MPC.

2.9. Angiogenesis and biosafety of SM scaffold in vivo

It is well known that bone formation is inherently connected to angiogenesis [64,65]. The presence of newly-generated trabeculae aligned with osteoblasts was accompanied by the presence of new blood vessels, as indicated by the red arrows (Fig. 8C and D). The presence of more blood vessels in the SM-35 group provided further evidence of the exceptional bone-healing capacity of SM scaffold. Subsequently, the expression of CD31 was detected by immunofluorescence staining, which was performed to further validate the angiogenic effects of SM scaffold. Consistently, more cells in SM-35 group were strongly immunostained with the anti-CD31 than in MPC at 12 weeks (Fig. 8G and J).

Finally, systemic toxicity of SM scaffold was tested at the 4 and 12 weeks after transplantation, and no obvious inflammatory lesions were found (Figs. S12A and B). In addition, we analyzed the postoperative blood biochemistry and electrolyte levels of the rats, and the results were all within the normal range (Fig. S13). These confirmed the *in vivo* biosafety of SM-35 and MPC in rats. What's more, regarding the concentration of serum Mg^{2+}, our findings indicated that there was no significant distinction between MPC and SM-35 (Fig. S14).

3. Conclusion

This study involved the fabrication of a novel MPC that incorporated nanofibers. The introduction of SF nanofibers resulted in enhanced mechanical quality that might be advantageous for *in vivo* strength while simultaneously reducing the potential for tissue damage. More importantly, the SF nanofibers caused hierarchically pore structure and reduced the pH of MPC, thereby promoting cell adhesion, spreading, proliferation, osteogenesis and angiogenesis. Moreover, the bone defect model of rat calvaria proved that the novel MPC exhibited enhanced osteogenesis, bone ingrowth and vascularization. These enhanced performances might be regulated by inhibiting the Notch signaling pathway. Collectively, these findings provided compelling evidence the novel MPC has significant potential for use in bone defect repair.

4. Materials and methods

4.1. Chemicals and materials

Magnesia (MgO) with a purity of 98.5% and potassium dihydrogen phosphate (KH_2PO_4) with a purity of 99.5% were purchased from Sinopharm Chemical Reagent CO., Ltd. (Shanghai, China). The silk cocoons of the Bombyx mori species were acquired from Hubei Cellamatrix Co., Ltd. (Wuhan, Hubei, China).

4.2. Preparation of SF

To extract sericin from the cocoons, 10 g of Bombyx mori cocoons were degummed by boiling in 4 L of sodium carbonate solution (0.02 M) at 90–100 °C for 30 min. Refined SF fibers were produced by baking at 60 °C. The SF fibers were dispersed in 9.3 M aqueous lithium bromide for 4 h at 60 °C. The resulting solution was then inserted into a dialysis tube (3500 MWCO) and dialyzed for 4 days against deionized water, with the water being replaced every 12 h to eliminate lithium bromide. The SF was finally prepared by freeze-drying for 48 h and then stored at 4 °C for subsequent investigations.

4.3. Fabrication of SF nanofibers

SF was dissolved in hexafluoroisopropanol (HFIP) for 12 h, yielding a 7 wt percent (wt%) electrospinning solution. A 10 mL syringe was filled with the solution and put into a single-channel syringe pump. The needle was 15 cm from the receiving plate, and the working voltage was 16 kV. To create an electrospun SF mat on aluminum foil, the syringe was driven at a rate of 0.8 mL/h. The resulting electrospun mats were submerged in absolute ethanol for crosslinking, then vacuum-dried in an oven for 72 h. The crosslinked SF was embrittled with frozen nitrogen for 10 min, followed by promptly grinding in a mortar. THF-SEM (Tescan VEGA Compact, Tescan, Brno, Czech Republic) was used to examine the morphology of the SF electrospun mats. The typical diameter of 100 NFs was determined by Image J (NIH, Bethesda, MD, USA).

4.4. Fabrication of SM

SM includes solid and liquid phases. The solid phase is composed of dead burned MgO (calcined at 1600 °C for 4 h), KH_2PO_4 (at a molar ratio of 1:1.5 with MgO) and short SF (15%, 25%, 35% or 45% (wt%) of the solid phase). The molar ratio of 1.5:1 was selected on the basis of our previous study [15,17]. After repeated trials, we found that the cement of molar ratio of 1.5:1 possessed well anti-washout property, lower pH and suitable setting time. In a tiny beaker, the mixture were combined and swirled, and then subjected to a 5-min ultrasonication. The solid and liquid phases (deionized water) were thoroughly mixed with a powder to liquid ratio of 2:1 (P/L, g/mL), and the homogeneous paste was then transferred to cylindrical molds. The fabricated cements were self-set at 37 °C and 100% relative humidity for 72 h. The composition of cements is listed in Table 1.

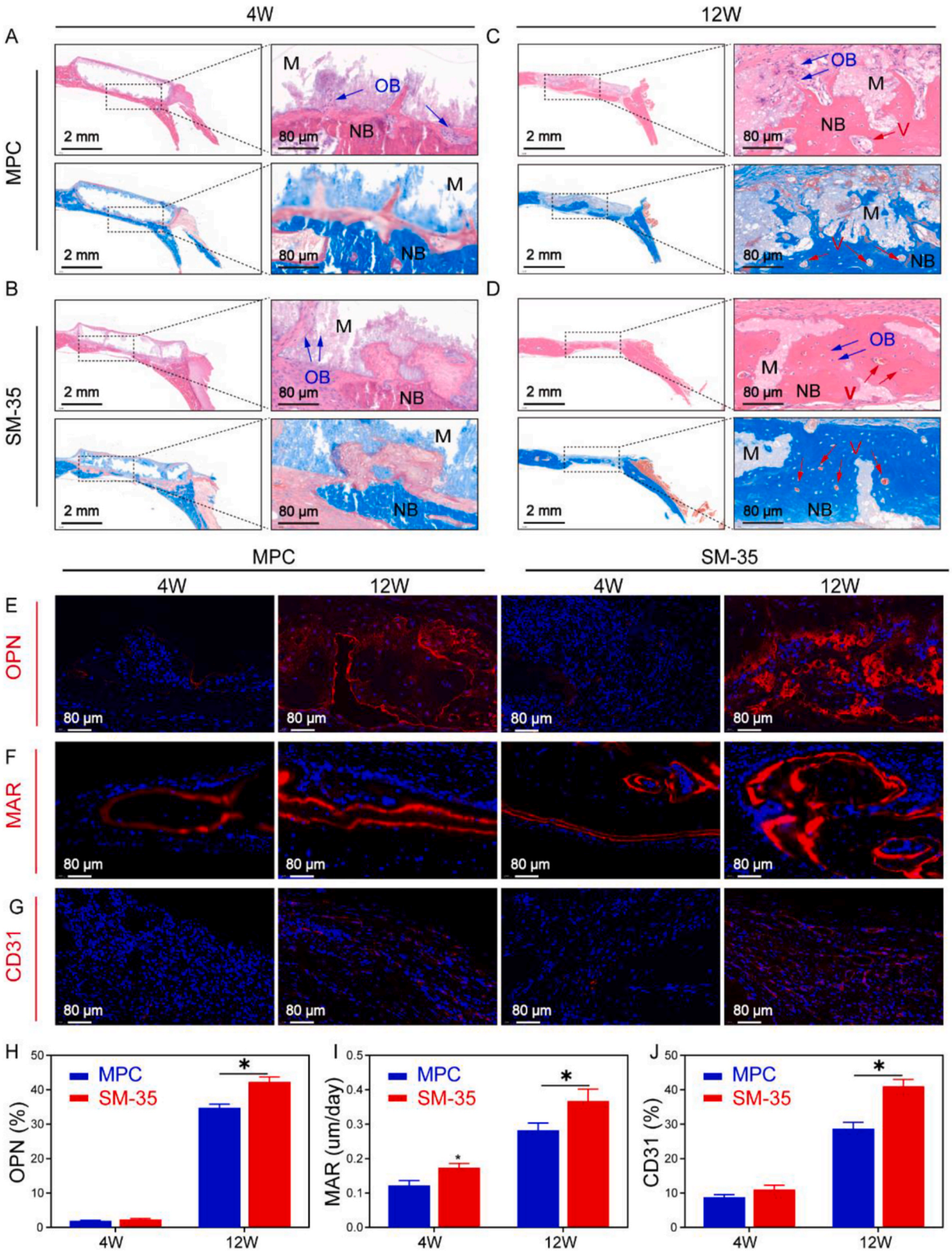

Fig. 8. H&E, Masson's trichrome staining and fluorescent labeling of rat cranial sections of regenerated bone observed at 4 and 12 weeks following implantation. (A) Four weeks after MPC transplantation. (B) Four weeks after SM-35 transplantation. (C) Twelve weeks after MPC transplantation. (D) Twelve weeks after SM-35 transplantation. M: materials, NB: new bone formation, OB; osteoblasts (blue arrows), V: new vascular formation (red arrows). (E) Immunofluorescent staining of OPN at 4 and 12 weeks after operation. (F) Typical fluorescence microscopic images of alizarin red staining 4 and 12 weeks after surgery. (G) Immunofluorescent staining of CD31 at 4 and 12 weeks after operation. (H) Quantitative analysis of OPN. (I) Quantitative analysis of mineral apposition rate (MAR). (J) Quantitative analysis of CD31. The data are shown as mean ± SD with a specimen number of at least three; statistical significance compared to the MPC group, $*p < 0.05$, $**p < 0.01$ and $***p < 0.001$.

Table 1
The composition of SF/MPC (SM).

Solid phase	Molar ratio (KH_2PO_4/MgO)	Liquid phase	P/L (g/mL)	SF (Wt %)
MPC	1:1.5	deionized water	2 g/mL	0
SM-15	1:1.5	deionized water	2 g/mL	15%
SM-25	1:1.5	deionized water	2 g/mL	25%
SM-35	1:1.5	deionized water	2 g/mL	35%
SM-45	1:1.5	deionized water	2 g/mL	45%

4.5. Chemical composition and surface morphology

The phase composition was analyzed by XRD (SmartLab, Rigaku, Tokyo, Japan), performed using CuKα radiation at 40 kV and 50 mA over a 2θ range of 10–65° and FTIR (Thermo FTIR5700; Thermo Fisher Scientific, Waltham, MA, USA). For FTIR, the samples were crushed into a tablet with KBr powders and tested using a single reflection ATR-OMNI sampler from 4000 to 500 cm^{-1}. XPS (Thermo Fisher 250Xi, USA) was used to analyze the elemental composition and valence state of the samples. The XPS analysis was conducted using a 30.0 eV analyser mode. The surface morphology of the cement samples was examined by THF-SEM and the elemental distribution on the surface of the sample was examined in SEM images using EDS.

4.6. Rheological behavior measurement

The rheological behavior measurement of cements were conducted by a rotational rheometer (Kinexus Pro$^+$, Malvern, Shanghai, China). Each phase was mixed according to the designed ratio (Table 1) and the obtained slurry was transferred to the rheometer for test. The Bingham model was applied to annotate the rheological behavior of each sample based on rheological measurement results.

4.7. Setting time and temperature measurement

The determination of solidification time, as outlined in the Chinese National Standard (GB/T1346-2001). The initial setting time refers to the period starting from the moment when two phases are mixed together until the Vicat apparatus needle is less than 5 mm away from the bottom. The final setting time is determined by using a Vicat instrument to measure the duration until a needle fails to penetrate the sample by more than 1 mm. The temperature variation of the paste during the hydration process was examined using a thermal infrared imaging instrument. Once the paste was poured into the mold for a duration of 45 s, the thermal infrared imaging device was securely positioned at a height of 15 cm on the top of the mold. Subsequently, the device documented the temperature of the paste at 15-s intervals. At least three repetitions were conducted.

4.8. Compressive strength analysis and porous structure evaluation

The compressive strength experiment follows the guidelines stated in ISO13779-1. The samples (Φ 6 mm × 12 mm) used for compressive strength testing were subjected to a standard curing technique for 72h at a temperature of 37 °C and with 100% humidity. This was done to ensure that the hydration reaction was fully completed. Afterwards, a universal material testing machine (SHT4 605, MTS Systems, Eden Prairie, MN, USA) was used to evaluate the compressive strength in wet conditions, with a loading rate of 1 mm/min. MicroActive AutoPore V9600 (Micrometrics Instrument Corporation, Norcross, GA, USA) was utilized to conduct the mercury intrusion porosimetry (MIP) test for evaluating the pore size distribution and porosity of the cements. At least three repetitions were conducted.

4.9. pH variation and degradation behavior in vitro

All of the cements (Φ6 mm × 12 mm) were submerged in 20 mL/g of phosphate-buffered saline (PBS, pH = 7.4) and incubated at 37 °C with shaking at 80 rpm. At day 1, 3, 5, 7, 14, 21 and 28, the pH of the PBS solution was measured using a pH meter (PHS-25; INESA, Shanghai, China). At least three repetitions were conducted.

To evaluate the degradation characteristics of different scaffolds, the initial mass of these samples was recorded as M_0. The samples (Φ6 mm × 12 mm) were submerged in PBS (pH = 7.4) or SBF at a concentration of 20 mL/g and then agitated in a shaking incubator at 37 °C at a speed of 80 rpm. Subsequently, the cement samples underwent a rinsing process using deionized water and were subjected to drying conditions at a temperature of 60 °C for a duration of 12 h. The mass of each sample at the indicated time-points was measured and recorded as M_1. The degradation rate was calculated as the percentage of the weight loss (L, (%)) to the initial weight, which is $L = \frac{M0-M1}{M0} \times 100\%$. At least three repetitions were conducted.

As for Mg^{2+} measurement, samples (Φ6 mm × 12 mm) were submerged in PBS (pH = 7.4) at a concentration of 20 mL/g and then agitated in a shaking incubator at 37 °C at a speed of 80 rpm, then atomic absorption spectrophotometer (contrAA700, Analytik Jena AG, Jena, Germany) was utilized to document the concentration of Mg^{2+} of 100 μL buffer from the solution at day1, 2, 3, 4 and 5, respectively.

4.10. In vitro studies

4.10.1. Biocompatibility of bone cements assessed by live-dead and CCK-8 assay

Rat bone marrow mesenchymal stem cells (BMSCs) were purchased from Wuhan Servicebio Technology Co., Ltd. (Wuhan, China) and cultured in complete medium of rat BMSCs (STCC5011 M) in a constant temperature incubator at 37 °C with 5% CO_2. When the density of BMSCs reached 80–90%, they were subcultured. The third to eighth generation cells were used for follow-up experiments.

Prior to cell seeding, all samples (Φ6 mm × 12 mm) were sterilized. In order to evaluate the biocompatibilities of the bone cements, a live–dead staining kit was utilized (Dalian Meilun Biotechnology Co. Ltd., Dalian, China). In a 48-well plate, 1×10^4 BMSCs were seeded onto bone cements, and 2 mL of medium was added to each well. On the third day, cements were treated with 2 μM calcein-AM (to stain living cells) and 8 μM propidium iodide (PI; to stain dead cells) for 30 min at 37 °C. Following a PBS rinse, the cells were observed under an Olympus IX71 fluorescence microscope (Olympus, Tokyo, Japan).

The proliferation of BMSCs co-cultured with different cements was evaluated using the Cell Counting Kit-8 (CCK-8) provided by Dojindo Laboratories (Kumamoto, Japan). The cells were seeded at a density of 10^4 cells per well and subsequently incubated for 1, 3, or 5 days. The cells were then subjected to 10 μL of CCK-8 at a temperature of 37 °C for 2 h. Assessment of the viability of BMSCs was conducted at a wavelength of 450 nm using a microplate reader. Cell viability was determined by calculating the OD values using the formula: Cell viability = $(OD_{treat} - OD_{blank})/(OD_{control} - OD_{blank}) \times 100\%$, where treat referred groups MPC, SM-15, SM-25 and SM-35, control referred no cement was added in the medium of day1, 3 and 5, respectively, blank referred no cement nor medium. The viability ≥70% indicated the good quality.

4.10.2. Cell attachment and morphology

Bone cements co-cultured with BMSCs were observed by THF-SEM. Samples were fixed with 4% paraformaldehyde, dehydrated with graded alcohol and dried in an oven at 60 °C. Then they were fixed on the sample stage, gold-plated with an ion sputtering instrument, and

finally scanned by THF-SEM at different magnifications.

The morphology of BMSCs on the cements was assessed by cytoskeletal staining with TRITC–phalloidin (G1041, Wuhan Servicebio Technology Co. Ltd., Wuhan, China). The nuclei of BMSCs were counterstained with 4',6-diamidino-2-phenylindole (DAPI). Finally, a fluorescence microscope (Olympus IX71) was used to observe and capture the fluorescent images.

4.10.3. Osteogenic differentiation of BMSCs

BMSCs were cultured with bone cements at a concentration of 10^5 cells per milliliter in basic culture medium. Once the cells reached a density of around 70%, they were then cultured with osteogenic induction medium (OIM) to initiate the differentiation process for a duration of either 14 or 21 days. The differentiation was assessed by means of ALP staining, measurement of ALP activity and ARS staining. These evaluations were conducted following the instructions provided with the ALP and ARS assay kits (Beyotime, China) and the results were observed under a light microscope (Olympus IX71).

4.10.3.1. Western blotting analysis. Protein lysis buffer (Beyotime, Beijing, China) was used to extract proteins from BMSCs after 14 days of co-culture in OIM. The protein concentration was measured using Bicinchoninic Acid (BCA). A total of 40 μg protein was separated using SDS-PAGE and transferred onto a PVDF membrane. After blocking with 5% skimmed milk, the appropriate primary antibodies (anti-bone morphogenetic protein 2 (BMP2) antibody (GB11252), anti-osteopontin (OPN) antibody (GB112328), anti-Runt-related transcription factor (RUNX2) antibody (GB13264), anti-Hey2 antibody (GB114277), anti-NICD antibody (GB11690) or anti-Hes1 antibody (GB112254) were added and incubated overnight at 4 °C. After three rinses with Tris buffered saline and Tween-20, the membranes were incubated with a 1:3000 dilution of horseradish peroxidase secondary antibody for 2 h at room temperature. The PVDF membranes were treated with a luminous chemical in a dimly-lit setting to stimulate color development, and the results were analyzed. At least three repetitions were conducted. The antibodies used in this work came from Wuhan Servicebio Technology Co. Ltd. GAPDH was set as the internal reference gene.

4.10.3.2. Quantitative real-time PCR (qRT-PCR). The PRISM 7900HT sequence detection system (Applied Biosystems, Foster City, CA, USA) was used to conduct qRT-PCR. TRIzol reagent (15596026; Invitrogen, Carlsbad, CA, USA) was used to extract total RNA, and the RevertAid™ first strand cDNA synthesis kit (K1622; Thermo Fisher Scientific) was used to create cDNA. The expression of genes was standardized to GAPDH by the $2^{-\Delta\Delta CT}$ approach. Supplementary Table 1 provides a list of the primer sequences.

4.10.4. Tube formation assay

The HUVECs were deprived of nutrients overnight in High Glucose Dulbecco's Modified Eagle Medium (HG-DMEM) supplemented with 0.2% Fetal Bovine Serum (FBS). In order to assess the ability to form new blood vessels, we combined growth factor decreased Matrigel (BD Biosciences, San Jose, CA) with media that had been cultured with cement for 24 h (in a 1:1 ratio, volume to volume) in 24-well plates. The mixture was then allowed to solidify for 1 h. Cells (1×10^5/well) were subsequently seeded onto the Matrigel surface and cultivated in a medium supplemented with cement for a total of 24 h, with an initial incubation period of 12 h. Microscopic images were randomly captured using Image J with the Angiogenesis Analyzer (NIH, Bethesda, MD) to measure the tubular network. The criteria used for quantification were the number of primary nodes and the total segment length.

4.10.5. Transwell assay

HUVECs were seeded on the top chamber of the Transwell devices and cultured in a medium without serum. The cement-cultured medium for 24 h was introduced into the lower chamber. Following a 12-h incubation period at a temperature of 37 °C, the cells located on the upper surface of the insert were eliminated. The cells that migrated to the lower surface of the insert were subsequently fixed, treated with a 0.1% crystal violet dye, and subjected to microscopic examination. The cell count was determined using ImageJ software.

4.10.6. Wound healing assay

HUVECs were seeded in 6-well plates at a concentration of 5×10^4 cells per square centimeter. After the cells reached 100% confluence, the monolayer was scraped using a sterile pipette tip to create a zone devoid of cells. Subsequently, the cells were exposed to cement-cultured media (24 h), and the wound area of the monolayer was assessed using microscopy after 24 h.

4.10.7. Lentiviruses and infection

The lentivirus used for overexpressing NICD1 and the associated control lentivirus were acquired from Genechem. In order to create cell lines that were consistently transduced, BMSCs were infected with the viral supernatant following the protocol provided by the manufacturer. The infected cells (named OE-NICD1 and sham-NICD1) were cultured for 48 h before selecting stable transfectants by adding puromycin (5 μg/mL) to the selection medium for two weeks. Subsequently, non-infected cells and infected or control cells were cultured with SM-35 scaffold (named SM-35, SM-35+OE-NICD1 or SM-35+sham, respectively). Finally, ALP staining, ALP activity assay, ARS staining, western blotting and qRT-PCR were performed at the appropriate time-points to evaluate osteogenic differentiation.

4.11. In vivo experiments of SM

4.11.1. Bilateral calvarial bone defect model

A total of 36 male Sprague–Dawley rats aged 8–10 weeks were randomized into three groups (n = 12) to undergo bilateral calvarial bone defect surgery. Group 1: no cement (control); group 2: MPC; group 3: SM-35. All *in vivo* studies performed in this study were approved by the Investigational Ethical Review Board of Renmin Hospital of Wuhan University (approval number: 20220702C). Rats were weighed, anesthetized, and fixed on a brain stereotaxic instrument. The surgical area of the calvaria was shaved and disinfected with iodine, then a 2.0 cm sagittal incision was made in the center of the scalp to expose the calvaria. Next, a 6 mm defect was created on the symmetrical bilateral calvaria using a dental drill. The corresponding cements were implanted into the calvarial defects, then the skin was sutured and disinfected with iodine. Finally, the rats were placed on a hot plate until their body temperature recovered, then they were raised continually in a cage. To assess mineral deposition, a fluorochrome label (30 mg/kg, alizarine, Beyotime) was administered at 14 days and 4 days before sacrifice. Meanwhile, blood was obtained for biochemical and electrolyte analysis. After 4 and 12 weeks of implantation, the cements and the surrounding bone, as well as the liver and kidneys, were harvested and dissected for further analysis.

4.11.2. Micro-computed tomography

The dissected samples were fixed and scanned by micro-computed tomography (micro-CT) using a ScanXmate-E090S40 system (Kanagawa, Japan). The scanning was performed with predetermined scanning settings, resulting in the acquisition of the original image. Subsequently, the designated region of interest in the initial image underwent reconstruction using the 3D reconstruction program NRecon (version V1.7.4.2, Bruker MicroCT, Kontich, Belgium). Subsequently, the region of interest in the reconstructed image was subjected to analysis using CTAnalyser (software version 1.20.3.0, Bruker MicroCT). Various parameters, including total tissue volume (TV), bone volume (BV), volume ratio (BV/TV), trabecular bone number (Tb.N), trabecular bone thickness (Tb.th), and trabecular separation (Tb.Sp), were

obtained.

4.11.3. Histological analysis

The harvested specimens were fixed with 4% paraformaldehyde, then embedded in paraffin to obtain non-decalcified paraffin samples. Subsequently, 10 μm sections were cut using a hard tissue microtome (Leica SP1600; Leica Bio-systems, Nussloch, Germany) for H&E or Masson's trichrome staining according to the manufacturer's protocol. Sections were visually examined using a digital camera (Olympus BX51).

4.11.4. Immunofluorescence analysis

The other specimens were fixed and decalcified in 10% EDTA. After antigen retrieval, 3% BSA solution was applied to the specified area of tissue. Then primary antibodies (anti-CD31 rabbit pAb (GB11063-2, 1:600) and anti-OPN rabbit pAb (GB11500, 1:500)) were added and incubated overnight at 4 °C. Next day, secondary antibody (Cy3 conjugated Goat Anti-Rabbit IgG (GB21303, 1:100)) was added and incubated at room temperature for 50 min. Next, DAPI staining solution was added and incubated at room temperature for 10 min. Finally, the slides were photographed under a fluorescence microscope (Olympus BX51).

4.12. Statistical analysis

Data are presented in the form of mean ± standard deviation, and all statistical analyses were performed using either GraphPad Prism 9.5 Software or Origin 2023b software. The differences among all samples were examined by Student's t-test, one-way or two-way analysis of variance (ANOVA), and a significance level of $p < 0.05$ was deemed to indicate statistical significance.

Funding statement

The present study was completed with the support of the Provincial Key Resaearch and Development Program of Hubei, China (No.2020BCB058) and Youth Science and Technology Talent Project of Hubei Province (2023DJC163).

Ethics approval and consent to participate

All *in vivo* experiments were reviewed and approved by the Investigational Ethical Review Board of Renmin Hospital of Wuhan University. The ethical committee had confirmed authors' compliance with all relevant ethical regulations.

CRediT authorship contribution statement

Jingteng Chen: Writing – review & editing, Writing – original draft, Visualization, Investigation, Formal analysis, Data curation. **Ling Yu:** Writing – review & editing, Writing – original draft, Validation, Formal analysis, Data curation. **Tian Gao:** Writing – review & editing, Validation, Resources, Data curation, Conceptualization. **Xiangyang Dong:** Writing – review & editing, Visualization. **Shiyu Li:** Data curation. **Yinchu Liu:** Data curation. **Jian Yang:** Resources. **Kezhou Xia:** Resources. **Yaru Yu:** Data curation. **Yingshuo Li:** Data curation. **Sen Wang:** Data curation. **ZhengFu Fan:** Writing – review & editing, Writing – original draft, Validation, Resources, Conceptualization. **Hongbing Deng:** Writing – review & editing, Visualization, Supervision, Software, Conceptualization. **Weichun Guo:** Writing – review & editing, Writing – original draft, Validation, Supervision, Funding acquisition, Conceptualization.

Declaration of competing interest

The authors declare that they have no known competing financial interests or personal relationships that could have appeared to influence the work reported in this paper.

Appendix A. Supplementary data

Supplementary data to this article can be found online at https://doi.org/10.1016/j.bioactmat.2024.03.021.

References

[1] B. Wildemann, A. Ignatius, F. Leung, L.A. Taitsman, R.M. Smith, R. Pesantez, M. J. Stoddart, R.G. Richards, J.B. Jupiter, Non-union bone fractures, Nat. Rev. Dis. Prim. 7 (2021) 57, https://doi.org/10.1038/s41572-021-00289-8.
[2] A.H. Schmidt, Autologous bone graft: is it still the gold standard? Injury 52 (Suppl 2) (2021) S18–S22, https://doi.org/10.1016/j.injury.2021.01.043.
[3] E. Dondossola, P. Friedl, Host responses to implants revealed by intravital microscopy, Nat. Rev. Mater. 7 (2022) 6–22, https://doi.org/10.1038/s41578-021-00369-x.
[4] L. Chen, Y. Tang, K. Zhao, X. Zha, J. Liu, H. Bai, Z. Wu, Fabrication of the antibiotic-releasing gelatin/PMMA bone cement, Colloids Surf. B Biointerfaces 183 (2019) 110448, https://doi.org/10.1016/j.colsurfb.2019.110448.
[5] M. Zegre, E. Poljanska, L.A. Caetano, L. Goncalves, A. Bettencourt, Research progress on biodegradable polymeric platforms for targeting antibiotics to the bone, Int. J. Pharm. 648 (2023) 123584, https://doi.org/10.1016/j.ijpharm.2023.123584.
[6] R.Z. LeGeros, Calcium phosphate-based osteoinductive materials, Chem. Rev. 108 (2008) 4742–4753, https://doi.org/10.1021/cr800427g.
[7] J. Jeong, J.H. Kim, J.H. Shim, N.S. Hwang, C.Y. Heo, Bioactive calcium phosphate materials and applications in bone regeneration, Biomater. Res. 23 (2019) 4, https://doi.org/10.1186/s40824-018-0149-3.
[8] A. Vezenkova, J. Locs, Sudoku of porous, injectable calcium phosphate cements - path to osteoinductivity, Bioact. Mater. 17 (2022) 109–124, https://doi.org/10.1016/j.bioactmat.2022.01.001.
[9] K. Joyce, G.T. Fabra, Y. Bozkurt, A. Pandit, Bioactive potential of natural biomaterials: identification, retention and assessment of biological properties, Signal Transduct Target Ther 6 (2021) 122, https://doi.org/10.1038/s41392-021-00512-8.
[10] G.L. Koons, M. Diba, A.G. Mikos, Materials design for bone-tissue engineering, Nat. Rev. Mater. 5 (2020) 584–603, https://doi.org/10.1038/s41578-020-0204-2.
[11] E. O'Neill, G. Awale, L. Daneshmandi, O. Umerah, K.W. Lo, The roles of ions on bone regeneration, Drug Discov. Today 23 (2018) 879–890, https://doi.org/10.1016/j.drudis.2018.01.049.
[12] H. Zhou, B. Liang, H. Jiang, Z. Deng, K. Yu, Magnesium-based biomaterials as emerging agents for bone repair and regeneration: from mechanism to application, J. Magnesium Alloys 9 (2021) 779–804, https://doi.org/10.1016/j.jma.2021.03.004.
[13] S.A. Walling, J.L. Provis, Magnesia-based cements: a journey of 150 Years, and cements for the future? Chem. Rev. 116 (2016) 4170–4204, https://doi.org/10.1021/acs.chemrev.5b00463.
[14] B. Kanter, A. Vikman, T. Bruckner, M. Schamel, U. Gbureck, A. Ignatius, Bone regeneration capacity of magnesium phosphate cements in a large animal model, Acta Biomater. 69 (2018) 352–361, https://doi.org/10.1016/j.actbio.2018.01.035.
[15] L. Yu, K. Xia, C. Gong, J. Chen, W. Li, Y. Zhao, W. Guo, H. Dai, An injectable bioactive magnesium phosphate cement incorporating carboxymethyl chitosan for bone regeneration, Int. J. Biol. Macromol. 160 (2020) 101–111, https://doi.org/10.1016/j.ijbiomac.2020.05.161.
[16] C. Gong, S. Fang, K. Xia, J. Chen, L. Guo, W. Guo, Enhancing the mechanical properties and cytocompatibility of magnesium potassium phosphate cement by incorporating oxygen-carboxymethyl chitosan, Regen Biomater 8 (2021) rbaa048, https://doi.org/10.1093/rb/rbaa048.
[17] Y. Shi, L. Yu, C. Gong, W. Li, Y. Zhao, W. Guo, A bioactive magnesium phosphate cement incorporating chondroitin sulfate for bone regeneration, Biomed Mater 16 (2021), https://doi.org/10.1088/1748-605X/abf5c4.
[18] Y. Zhao, S. Yu, X. Wu, H. Dai, W. Liu, R. Tu, T. Goto, Construction of macroporous magnesium phosphate-based bone cement with sustained drug release, Mater. Des. 200 (2021), https://doi.org/10.1016/j.matdes.2021.109466.
[19] S. Yu, L. Liu, C. Xu, H. Dai, Magnesium phosphate based cement with improved setting, strength and cytocompatibility properties by adding Ca(H(2)PO(4))(2).H(2)O and citric acid, J. Mech. Behav. Biomed. Mater. 91 (2019) 229–236, https://doi.org/10.1016/j.jmbbm.2018.12.004.
[20] J. Xue, T. Wu, Y. Dai, Y. Xia, Electrospinning and electrospun nanofibers: methods, materials, and applications, Chem. Rev. 119 (2019) 5298–5415, https://doi.org/10.1021/acs.chemrev.8b00593.
[21] P. Cai, S. Lu, J. Yu, L. Xiao, J. Wang, H. Liang, L. Huang, G. Han, M. Bian, S. Zhang, J. Zhang, C. Liu, L. Jiang, Y. Li, Injectable nanofiber-reinforced bone cement with controlled biodegradability for minimally-invasive bone regeneration, Bioact. Mater. 21 (2023) 267–283, https://doi.org/10.1016/j.bioactmat.2022.08.009.
[22] F. Yongcong, T. Zhang, L. Liverani, A.R. Boccaccini, W. Sun, Novel biomimetic fiber incorporated scaffolds for tissue engineering, J. Biomed. Mater. Res. A. 107 (2019) 2694–2705, https://doi.org/10.1002/jbm.a.36773.
[23] J.K. Sahoo, O. Hasturk, T. Falcucci, D.L. Kaplan, Silk chemistry and biomedical material designs, Nat. Rev. Chem 7 (2023) 302–318, https://doi.org/10.1038/s41570-023-00486-x.

[24] P. Garside, W. Paul, Z. Xiaomei, The inherent acidic characteristics of silk, part II - weighted silks, e-Preservation Sci. 7 (2010).
[25] L. Fan, J.L. Li, Z. Cai, X. Wang, Bioactive hierarchical silk fibers created by bioinspired self-assembly, Nat. Commun. 12 (2021) 2375, https://doi.org/10.1038/s41467-021-22673-4.
[26] G.S. Hussey, J.L. Dziki, S.F. Badylak, Extracellular matrix-based materials for regenerative medicine, Nat. Rev. Mater. 3 (2018) 159–173, https://doi.org/10.1038/s41578-018-0023-x.
[27] N. Kasoju, U. Bora, Silk fibroin based biomimetic artificial extracellular matrix for hepatic tissue engineering applications, Biomed Mater 7 (2012) 045004, https://doi.org/10.1088/1748-6041/7/4/045004.
[28] Y. Cheng, G. Cheng, C. Xie, C. Yin, X. Dong, Z. Li, X. Zhou, Q. Wang, H. Deng, Z. Li, Biomimetic silk fibroin hydrogels strengthened by silica nanoparticles distributed nanofibers facilitate bone repair, Adv. Healthcare Mater. 10 (2021) e2001646, https://doi.org/10.1002/adhm.202001646.
[29] M. Li, Y. Wu, H. Li, C. Tan, S. Ma, J. Gong, L. Dong, W. Huang, X. Li, H. Deng, Nanofiber reinforced alginate hydrogel for leak-proof delivery and higher stress loading in nucleus pulposus, Carbohydr. Polym. 299 (2023) 120193, https://doi.org/10.1016/j.carbpol.2022.120193.
[30] S.K. Ramasamy, A.P. Kusumbe, L. Wang, R.H. Adams, Endothelial Notch activity promotes angiogenesis and osteogenesis in bone, Nature 507 (2014) 376–380, https://doi.org/10.1038/nature13146.
[31] B. Zhou, W. Lin, Y. Long, Y. Yang, H. Zhang, K. Wu, Q. Chu, Notch signaling pathway: architecture, disease, and therapeutics, Signal Transduct Target Ther 7 (2022) 95, https://doi.org/10.1038/s41392-022-00934-y.
[32] J.M. Kraus, D. Giovannone, R. Rydzik, J.L. Balsbaugh, I.L. Moss, J.L. Schwedler, J. Y. Bertrand, D. Traver, K.D. Hankenson, J.G. Crump, D.W. Youngstrom, Notch signaling enhances bone regeneration in the zebrafish mandible, Development 149 (2022), https://doi.org/10.1242/dev.199995.
[33] C. Wang, J. Shen, K. Yukata, J.A. Inzana, R.J. O'Keefe, H.A. Awad, M.J. Hilton, Transient gamma-secretase inhibition accelerates and enhances fracture repair likely via Notch signaling modulation, Bone 73 (2015) 77–89, https://doi.org/10.1016/j.bone.2014.12.007.
[34] S. Midha, S. Murab, S. Ghosh, Osteogenic signaling on silk-based matrices, Biomaterials 97 (2016) 133–153, https://doi.org/10.1016/j.biomaterials.2016.04.020.
[35] G. Cheng, J. Dai, J. Dai, H. Wang, S. Chen, Y. liu, X. Liu, X. Li, X. Zhou, H. Deng, Z. Li, Extracellular matrix imitation utilizing nanofibers-embedded biomimetic scaffolds for facilitating cartilage regeneration, Chem. Eng. J. 410 (2021), https://doi.org/10.1016/j.cej.2020.128379.
[36] L. Yu, T. Gao, W. Li, J. Yang, Y. Liu, Y. Zhao, P. He, X. Li, W. Guo, Z. Fan, H. Dai, Carboxymethyl chitosan-alginate enhances bone repair effects of magnesium phosphate bone cement by activating the FAK-Wnt pathway, Bioact. Mater. 20 (2023) 598–609, https://doi.org/10.1016/j.bioactmat.2022.06.017.
[37] E. Şahin, D.M. Kalyon, The rheological behavior of a fast-setting calcium phosphate bone cement and its dependence on deformation conditions, J. Mech. Behav. Biomed. Mater. 72 (2017) 252–260, https://doi.org/10.1016/j.jmbbm.2017.05.017.
[38] X. Lin, S. Patil, Y.G. Gao, A. Qian, The bone extracellular matrix in bone formation and regeneration, Front. Pharmacol. 11 (2020) 757, https://doi.org/10.3389/fphar.2020.00757.
[39] J. Melke, S. Midha, S. Ghosh, K. Ito, S. Hofmann, Silk fibroin as biomaterial for bone tissue engineering, Acta Biomater. 31 (2016) 1–16, https://doi.org/10.1016/j.actbio.2015.09.005.
[40] J. McLean, L. Cui, Multiscale geomechanical behavior of fiber-reinforced cementitious composites under cyclic loading conditions—a review, Front. Mater. 8 (2021), https://doi.org/10.3389/fmats.2021.759126.
[41] C. Zhu, C. Huang, W. Zhang, X. Ding, Y. Yang, Biodegradable-glass-fiber reinforced hydrogel composite with enhanced mechanical performance and cell proliferation for potential cartilage repair, Int. J. Mol. Sci. 23 (2022), https://doi.org/10.3390/ijms23158717.
[42] J. Zhang, W. Liu, V. Schnitzler, F. Tancret, J.M. Bouler, Calcium phosphate cements for bone substitution: chemistry, handling and mechanical properties, Acta Biomater. 10 (2014) 1035–1049, https://doi.org/10.1016/j.actbio.2013.11.001.
[43] M.H. Esnaashary, H.R. Rezaie, A. Khavandi, J. Javadpour, Evaluation of setting time and compressive strength of a new bone cement precursor powder containing Mg-Na-Ca, Proc. Inst. Mech. Eng. H. 232 (2018) 1017–1024, https://doi.org/10.1177/0954411918796048.
[44] Y. Zuo, F. Yang, J.G.C. Wolke, Y. Li, J.A. Jansen, Incorporation of biodegradable electrospun fibers into calcium phosphate cement for bone regeneration, Acta Biomater. 6 (2010) 1238–1247, https://doi.org/10.1016/j.actbio.2009.10.036.
[45] Y. Zuo, F. Yang, J.G. Wolke, Y. Li, J.A. Jansen, Incorporation of biodegradable electrospun fibers into calcium phosphate cement for bone regeneration, Acta Biomater. 6 (2010) 1238–1247, https://doi.org/10.1016/j.actbio.2009.10.036.
[46] K. Katalin, B. Attila, Comparative study of setting time and heat of hydration development of Portland cement according to EN 196-3, in: R.-A. José Luis, F.-H. Cynthia Graciela (Eds.), Applications of Calorimetry, IntechOpen, Rijeka, 2022. Ch. 4.
[47] S. Wei, J.X. Ma, L. Xu, X.S. Gu, X.L. Ma, Biodegradable materials for bone defect repair, Mil Med Res 7 (2020) 54, https://doi.org/10.1186/s40779-020-00280-6.
[48] J.-L. Wang, J.-K. Xu, C. Hopkins, D.H.-K. Chow, L. Qin, Biodegradable magnesium-based implants in orthopedics—a general review and perspectives, Adv. Sci. 7 (2020) 1902443, https://doi.org/10.1002/advs.201902443.
[49] W. Liu, X. Dan, W.W. Lu, X. Zhao, C. Ruan, T. Wang, X. Cui, X. Zhai, Y. Ma, D. Wang, W. Huang, H. Pan, Spatial distribution of biomaterial microenvironment pH and its modulatory effect on osteoclasts at the early stage of bone defect regeneration, ACS Appl. Mater. Interfaces 11 (2019) 9557–9572, https://doi.org/10.1021/acsami.8b20580.
[50] Z. Ding, W. Cheng, M.S. Mia, Q. Lu, Silk biomaterials for bone tissue engineering, Macromol. Biosci. 21 (2021) e2100153, https://doi.org/10.1002/mabi.202100153.
[51] M.A. Haque, B. Chen, In vitro and in vivo research advancements on the magnesium phosphate cement biomaterials: a review, Materialia 13 (2020) 100852, https://doi.org/10.1016/j.mtla.2020.100852.
[52] N. Abbasi, S. Hamlet, R.M. Love, N.-T. Nguyen, Porous scaffolds for bone regeneration, J SCI-ADV MATER DEV. 5 (2020) 1–9, https://doi.org/10.1016/j.jsamd.2020.01.007.
[53] R.A. Perez, G. Mestres, Role of pore size and morphology in musculo-skeletal tissue regeneration, Mater. Sci. Eng., C 61 (2016) 922–939, https://doi.org/10.1016/j.msec.2015.12.087.
[54] J. Li, J. Xia, L. Di Sarno, G. Gong, Fiber utilization in pervious concrete: review on manufacture and properties, Construct. Build. Mater. 406 (2023) 133372, https://doi.org/10.1016/j.conbuildmat.2023.133372.
[55] Y.J. Kim, A. Gaddafi, I. Yoshitake, Permeable concrete mixed with various admixtures, Mater. Des. 100 (2016) 110–119, https://doi.org/10.1016/j.matdes.2016.03.109.
[56] C.S. Chua, S.Y. Ow, S.L. Liew, J. Liu, C.B. Soh, L. Shen, S. Wang, 3D printing of fibre-reinforced ceramic composites with hierarchical structure, Adv. Appl. Ceram. 121 (2022) 46–51, https://doi.org/10.1080/17436753.2021.2014276.
[57] S.R. Jung, N.J. Song, D.K. Yang, Y.J. Cho, B.J. Kim, J.W. Hong, U.J. Yun, D.G. Jo, Y.M. Lee, S.Y. Choi, K.W. Park, Silk proteins stimulate osteoblast differentiation by suppressing the Notch signaling pathway in mesenchymal stem cells, Nutr. Res. 33 (2013) 162–170, https://doi.org/10.1016/j.nutres.2012.11.006.
[58] M.J. Hilton, X. Tu, X. Wu, S. Bai, H. Zhao, T. Kobayashi, H.M. Kronenberg, S. L. Teitelbaum, F.P. Ross, R. Kopan, F. Long, Notch signaling maintains bone marrow mesenchymal progenitors by suppressing osteoblast differentiation, Nat Med 14 (2008) 306–314, https://doi.org/10.1038/nm1716.
[59] F. Engin, Z. Yao, T. Yang, G. Zhou, T. Bertin, M.M. Jiang, Y. Chen, L. Wang, H. Zheng, R.E. Sutton, B.F. Boyce, B. Lee, Dimorphic effects of Notch signaling in bone homeostasis, Nat Med 14 (2008) 299–305, https://doi.org/10.1038/nm1712.
[60] C. Wang, J.A. Inzana, A.J. Mirando, Y. Ren, Z. Liu, J. Shen, R.J. O'Keefe, H. A. Awad, M.J. Hilton, NOTCH signaling in skeletal progenitors is critical for fracture repair, J. Clin. Invest. 126 (2016) 1471–1481, https://doi.org/10.1172/JCI80672.
[61] L.H. Remark, K. Leclerc, M. Ramsukh, Z. Lin, S. Lee, B. Dharmalingam, L. Gillinov, V.V. Nayak, P. El Parente, M. Sambon, P.J. Atria, M.A.E. Ali, L. Witek, A.B. Castillo, C.Y. Park, R.H. Adams, A. Tsirigos, S.M. Morgani, P. Leucht, Loss of Notch signaling in skeletal stem cells enhances bone formation with aging, Bone Res 11 (2023) 50, https://doi.org/10.1038/s41413-023-00283-8.
[62] T.L. Kivell, A review of trabecular bone functional adaptation: what have we learned from trabecular analyses in extant hominoids and what can we apply to fossils? J. Anat. 228 (2016) 569–594, https://doi.org/10.1111/joa.12446.
[63] B. Liu, J. Li, X. Lei, P. Cheng, Y. Song, Y. Gao, J. Hu, C. Wang, S. Zhang, D. Li, H. Wu, H. Sang, L. Bi, G. Pei, 3D-bioprinted functional and biomimetic hydrogel scaffolds incorporated with nanosilicates to promote bone healing in rat calvarial defect model, Mater. Sci. Eng., C 112 (2020) 110905, https://doi.org/10.1016/j.msec.2020.110905.
[64] K.K. Sivaraj, R.H. Adams, Blood vessel formation and function in bone, Development 143 (2016) 2706–2715, https://doi.org/10.1242/dev.136861.
[65] P. Qiu, M. Li, K. Chen, B. Fang, P. Chen, Z. Tang, X. Lin, S. Fan, Periosteal matrix-derived hydrogel promotes bone repair through an early immune regulation coupled with enhanced angio- and osteogenesis, Biomaterials 227 (2020) 119552, https://doi.org/10.1016/j.biomaterials.2019.119552.